

Interactions between a Developing Mesoscale Convective System and Its Environment. Part I: Observational Analysis

JASON E. NACHAMKIN,* RAY L. MCANELLY, AND WILLIAM R. COTTON

Department of Atmospheric Science, Colorado State University, Fort Collins, Colorado

(Manuscript received 17 March 1999, in final form 24 June 1999)

ABSTRACT

This paper is the first in a two part series in which the interactions between a growing mesoscale convective system (MCS) and its surrounding environment are investigated. The system studied here developed in north-eastern Colorado on 19 July 1993 and propagated into Kansas as a long-lived nocturnal MCS. High-resolution dual-Doppler and surface mesonet data collected from this system are discussed in Part I, while the results of a numerical simulation are discussed in Part II.

The observations show that organized mesoscale surface pressure and flow features appeared very early in the lifetime of this system, long before the development of any trailing stratiform precipitation. Most of the stratiform anvil advected ahead of the convective line in the strong upper-tropospheric westerlies. In accordance with this, most of the mid- and upper-tropospheric storm-relative flow behind the line remained westerly, or rear-to-front.

Despite the westerlies, the strongest flow perturbations with respect to the ambient winds developed to the rear of the line. The structure of these perturbations was similar to the upper-tropospheric front-to-rear and midtropospheric rear-to-front flows typically found in more mature leading-line/trailing-stratiform systems. The presence of these perturbations on the upwind side of the convective line indicates that gravity wave propagation was primarily responsible for their development.

1. Introduction

Moist convection is linked to its surrounding environment primarily through the propagation of gravity waves and advective outflows. For the most part, these disturbances rapidly weaken as they propagate away from an individual cell. However, if many convective cells become concentrated in a limited area for a long time, long-lived mesoscale circulations can develop (Rossby 1938). From a satellite perspective, organized systems appear as large shields of cold cirrus clouds and are often classified as a mesoscale convective system (MCS) or a mesoscale convective complex (MCC) depending on their shape, size, and duration (Maddox 1980).

For a long-lived MCS to occur, the atmosphere must support a focused group of convective storms. If significant instability exists over a large region, some combination of environmental and or physiographic factors

generally triggers convection in one area while suppressing it everywhere else. However, if convection is not localized, the instability is rapidly used up by numerous isolated cells. While it is possible that subsidence from initial convection may suppress additional storms, recent work by Mapes (1993) suggests that convection actually promotes additional development. Many MCSs, such as the one studied in this work, originate over the Rocky Mountains and adjacent high plains of eastern Colorado (McAnelly and Cotton 1986), where convection is effectively focused by the regional topography. Dirks (1969), Wetzel et al. (1983), and Tripoli and Cotton (1989) showed that initial convection often developed near mountaintop early in the day and propagated onto the plains. Once on the plains, Tripoli and Cotton (1989) noted that convection was effectively focused by the capping inversion. By providing a barrier to all but the strongest forcing, the cap allowed the buildup of convective available potential energy (CAPE) to be released in limited areas. The low-level jet in combination with a stationary frontal zone also play key roles in focusing and maintaining nocturnal convection as it propagates away from the mountains (Maddox 1983; Trier and Parsons 1993).

As an MCS develops, the individual cells group into clusters or lines depending on the nature of the focusing and the ambient shear (Bluestein and Jain 1985; Houze

* Current affiliation: Naval Research Laboratory, Monterey, California.

Corresponding author address: Dr. Jason Nachamkin, Naval Research Laboratory, 7 Grace Hopper Ave., Monterey, CA 93943.
E-mail: nachamkin@nrlmry.navy.mil

et al. 1990). Stratiform precipitation also develops and is often found trailing the convective line (Houze et al. 1989). Asymmetries in the stratiform precipitation structure can develop (Houze et al. 1990), and occasionally the stratiform anvil advects ahead of the line (Grady and Verlinde 1997). Many mature MCSs with large stratiform cloud shields contain unified mid- and upper-tropospheric flows that are on the scale of the entire system. These flows, in the form of the front-to-rear flow and rear inflow jet (Smull and Houze 1987; Houze et al. 1989), are nearly ubiquitous in the quasi-two-dimensional squall-line system. Other systems with more complex convective organization also exhibit similar features (Stumpf et al. 1991; Fortune et al. 1992; Smull and Augustine 1993; Nachamkin et al. 1994).

Nachamkin et al. (1994) and McAnelly et al. (1997) use the term "upscale growth" to describe the processes by which an MCS becomes organized on the mesoscale. The development of the mesoscale flow circulations is central to the upscale growth question, and processes within the contiguous stratiform precipitation region can contribute significantly to these circulations. LeMone (1983) showed that a midtropospheric, hydrostatic low forms due to heating within the rearward leaning convective towers. Brown (1979) and Smull and Houze (1987) pointed out that the combination of general latent heating within the stratiform anvil and cooling near the melting level combine to lower the midtropospheric pressure and in turn draw in midlevel rear inflow. Leary and Houze (1979) and Smull and Houze (1987) demonstrated that melting and evaporative cooling can also aid in the descent of the rear inflow. Lafore and Moncrieff (1989) attributed rear inflow to a horizontal rear-to-front pressure gradient in the midtroposphere beneath the stratiform region. Weisman (1992) hypothesized that horizontal buoyancy gradients along the back edge of an expanding convective system create a circulation that draws in midtropospheric air from behind the system.

These mechanisms imply that mesoscale flows would not develop in the absence of highly tilted convective towers, or a large stratiform anvil. However, evidence is increasing that these circulations can propagate into the clear air surrounding a group of convective cells. When convection perturbs the atmosphere, compensating motions propagate outward from the initial disturbance in the form of internal gravity waves. Bretherton and Smolarkiewicz (1989), Nicholls et al. (1991), Pandya et al. (1993), Mapes (1993), Pandya and Durran (1996), and McAnelly et al. (1997) have described these waves in the linearized, analytic solution, while Bretherton and Smolarkiewicz (1989), Schmidt and Cotton (1990), and Pandya and Durran (1996) have demonstrated their existence in two-dimensional, explicit, nonlinear convective models. Horizontal circulations associated with these waves closely resemble the front-to-rear and rear-to-front flows described by Houze et al. (1989), and may thus contribute to these flows.

Direct observational evidence of gravity waves on

the storm scale is limited for several reasons. As the waves propagate away from a system, the vertical motion along the wave fronts becomes distorted and is difficult to detect. Conventional measuring systems such as soundings and profiles are not sensitive enough to observe them. However, since the horizontal wave velocity perturbations are large in scale, they are easier to measure. Johnson et al. (1995) have observed horizontal perturbations in the clear air outside of a developing MCS that resembled those described by Mapes (1993). As an MCS grows large, any circulations generated within the stratiform anvil will be superimposed upon any preexisting wave-induced perturbations. Thus, separating features generated by these forcing mechanisms in a large, mature system is quite difficult. The best chance to observe the relative contributions from each component comes while the system is initially developing.

One of the main goals of this work is to observe the process by which developing convection within an MCS interacts with the surrounding atmosphere to produce a larger-scale disturbance. In this paper, the synoptic and mesoscale MCS environment, as well as the structure and evolution of the MCS, will be discussed using Doppler radar, surface mesonet, standard National Weather Service (NWS), and satellite observations. The observed storm-generated mesoscale circulations will be compared to the gravity wave structures found by Nicholls et al. (1991), Mapes (1993), and Pandya and Durran (1996). In Nachamkin and Cotton (2000, hereafter Part II), the simulated MCS and its environment will be compared to the observations in Part I. Since the gravity waves were explicitly resolved in the model, the actual development of the circulations will be tracked.

2. Data and analysis methods

a. Field project data

A small field project covering most of northeastern Colorado (Fig. 1) was conducted during late July and early August of 1992–94 (McAnelly et al. 1997), with the goal of collecting comprehensive observations of the MCS genesis process. Reflectivity and velocity data out to a range of 150 km were collected from the Colorado State University–University of Chicago and University of Illinois, Champaign (CSU–CHILL) radar (Rutledge et al. 1993), and the Next Generation Radar (NEXRAD) prototype Mile High (MH) radar (Pratte et al. 1991). During operations, synchronized volume scans were collected at 6-min intervals, with additional low-level surveillance scans out to a range of 252 km. For the 19–20 July 1993 case, volume scan data were collected from 2209 UTC (all times UTC¹) 19 July to

¹ To convert to local standard time, subtract 7 h from UTC time.

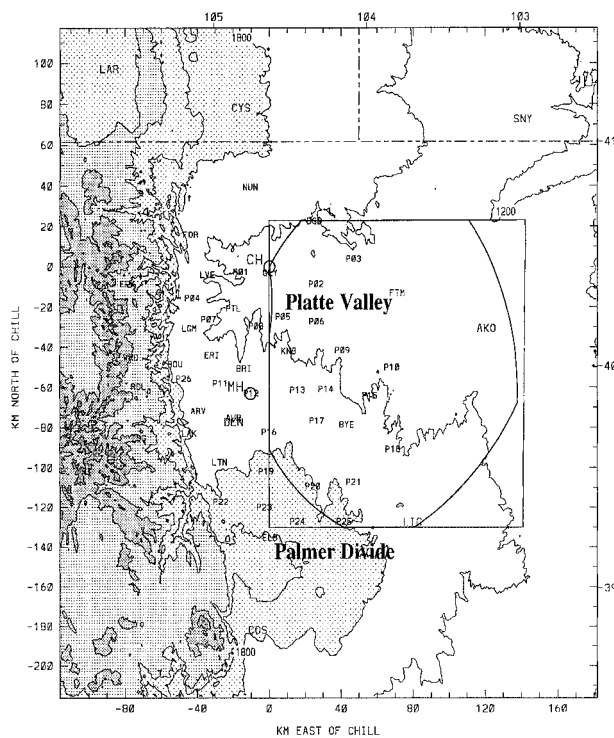


FIG. 1. The high-resolution data collection network used for the northeastern Colorado field project. PROFS mesonet stations and NWS hourly reporting stations are indicated by their three-letter identifiers in small and large font, respectively. NCAR PAM stations are indicated by a P followed by the station number. The radar analysis grid superimposed on the eastern Doppler lobe is indicated by the rectangle, and the circles labeled CH and MH depict the positions of the CSU-CHILL and Mile High Radars, respectively. Topography is contoured at the 1200, 1500, 1800, 2100, 2400, 3000, and 3600 m MSL levels and shaded at 1800, 2400, 3000, and 3600 m MSL. The left and bottom axes are labeled in km from the CSU-CHILL, while the top and right axes are labeled in longitude and latitude, respectively. Dashed lines indicate state boundaries.

0000 20 July, and surveillance scans were collected until 0145.

The radars were on a 64-km north-south baseline, and the resulting Doppler lobes were constrained rather liberally by the 20° beam crossing angle and the maximum volume scanning ranges of approximately 150 km (beamwidths of ~ 2.5 km) (Fig. 1). In this configuration, the lobes were well placed to observe convection as it moved off the high terrain and onto the plains. Storm-scale features were investigated while systems were closer to the radars. At far ranges, however, the center of the lowest beam was 2.5 km above ground level (AGL), and the resolution was quite coarse due to beam broadening. Therefore, much of the analysis will concentrate on the development of broad mid- and upper-tropospheric mesoscale flow regions. Such features are well sampled despite the coarse resolution (McAnelly et al. 1997).

In addition to NWS surface and upper-air sounding data, surface mesonet data were collected from stations

in two overlapping networks (Fig. 1). The first, supported by the National Oceanic and Atmospheric Administration Forecast Systems Lab, was formally known as the Program for Regional Observing and Forecasting Services (PROFS) mesonet. The second consisted of 26 Portable Automated Mesonet (PAM) stations operated by the National Center for Atmospheric Research (NCAR) for the Real-time Analysis and Prediction of Storms (RAPS-93) field project. The average station separation in the combined network was about 20 km. Measurements of pressure, temperature, dewpoint, wind speed and direction, maximum wind gust, and rain rate were recorded every 5 min and relayed back to forecasters in real time. The result was a high-resolution mesh of surface data through most of the western half of the Doppler analysis region. In epilogue, neither one of these networks is currently in full operation. These data were valuable forecasting and analysis tools and the authors lament their loss.

b. Analysis techniques

Twelve dual-Doppler analysis volumes were created for the following times: 2209, 2227, 2233, 2239, 2245, 2251, 2257, 2309, 2315, 2321, 2333, and 2345. Reflectivity and velocity data from each radar were manually edited and unfolded using the NCAR Research Data Support System software package (Oye and Carbone 1981). These data were then interpolated to the Cartesian analysis grid in Fig. 1 using SPRINT (Miller et al. 1986), and further processed with the CEDRIC (Mohr et al. 1986) software. The grid covered $141 \text{ km} \times 151 \text{ km}$ in the x and y directions with a spacing of 1.5 km. In the vertical, the grid extended from 2.5 km above mean sea level (MSL) ($\sim 1 \text{ km AGL}$) to 15 km MSL at intervals of 0.5 km.

As in Nachamkin et al. (1994), velocity data from each radar were combined by iteratively adjusting the horizontal and vertical wind components through the downward integration of the anelastic continuity equation. Variational techniques were not feasible due to the inadequate sampling of the lower domain. Prior to the vertical integration, the horizontal wind components were smoothed using a two-step Leise filter (Leise 1981). Features with wavelengths smaller than $4\Delta x$ (6 km) were strongly damped. Particle fall speed was accounted for by assuming different fall speeds for ice and water above and below the 0°C level, respectively. This level was determined from the 1200 19 July Denver (DEN) sounding to be 4.2 km MSL.

Doppler pressure retrievals were conducted using methods derived by Gal-Chen (1978) and software discussed in Parsons et al. (1987). The environmental mean virtual potential temperature profile was obtained from the 1200 19 July DEN sounding. The local time derivative terms were calculated using two volume scans separated by 6–12 min. Error values as described by Gal-Chen and Hane (1981) were less than 0.4 for the

data used herein. Additional details are as in Nachamkin (1998).

The raw mesonet pressure data were adjusted to 1500 m MSL using the standard atmospheric lapse rate. Individual station biases were then removed through comparison with surrounding NWS stations during several quiescent periods within one day of this case. Most of these corrections were on the order of 1 hPa or less; however, the four stations in the western foothills (EPK, WRD, ROL, and ISG) were excluded from the analyses due to high variabilities in their station pressure biases. Perturbations associated with the diurnal tide did not significantly contribute to the trends over the 2–3-h mesonet analysis periods and were, thus, not removed.

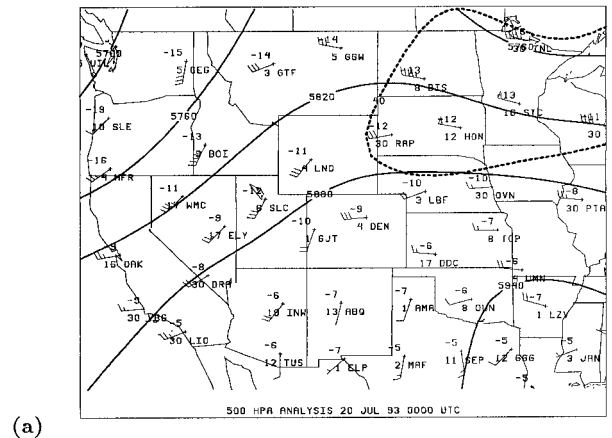
3. Synoptic conditions

At 0000 20 July, an anomalously deep upper-tropospheric trough was located off the United States west coast (Fig. 2a). This general pattern was locked in place for most of the summer of 1993 and was partially responsible for widespread flooding associated with repeated central plains MCS activity (Bell and Janowiak 1995). Some of these systems, including the 19–20 July case, originated in the high plains and grew large as they propagated eastward. McAnelly and Cotton (1986) described this type of evolution in detail for an MCC episode that occurred in 1977.

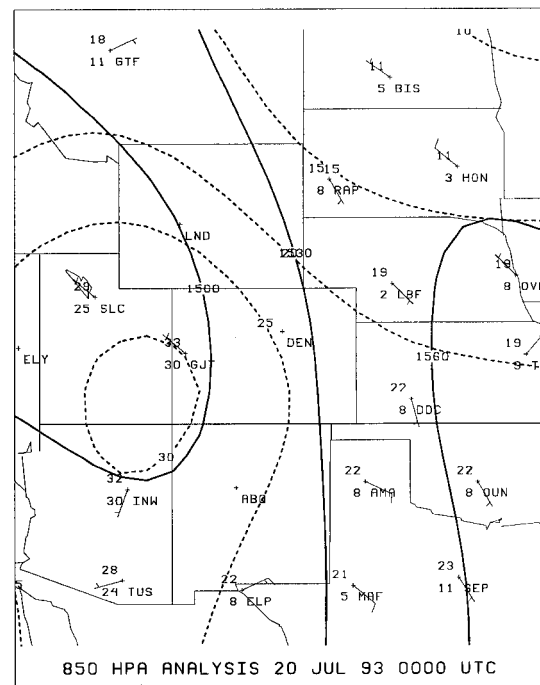
Northeastern Colorado was beneath the right entrance region of a 200-hPa jet streak, and wind speeds were about 35 m s^{-1} . At 500 hPa (Fig. 2a), the flow was generally $10\text{--}15 \text{ m s}^{-1}$, making for considerable upper-tropospheric shear. Composites by Maddox (1983) and Laing (1997) showed that upper-tropospheric jet streaks with moderate shear and baroclinicity were common to MCC environments. At 850 hPa (Fig. 2b), a seemingly weak low-level jet extended from southern Texas into Wyoming. Southeasterly flow brought moist air into the high plains ahead of low pressure located over southern Idaho. Although the measured winds at each station were only 10 m s^{-1} , model results discussed in Part II of this work suggest that an intense but small-scale jet formed in southeastern Colorado between the reporting stations. Although speeds within this jet were up to 20 m s^{-1} , the jet core was only 100 km across.

At the surface, an ill-defined quasi-stationary front stretched eastward from Colorado (Fig. 3). Through the day, this front slowly moved northward through eastern Colorado and western Kansas. Southeasterly gradient flow combined with diurnal upslope brought deep moisture westward from the rain-soaked plains. Dewpoints in northeastern Colorado were anomalously high as a result, with values in many areas at or above 15°C .

The convective potential is best viewed with the 1200 19 July DEN sounding (Fig. 4), since the 0000 sounding was in the wake of the convective system. At 1200 the bulk of the lower-tropospheric moisture extended from the surface to about 777 mb ($\sim 700 \text{ m AGL}$). Modified



(a)



(b)

FIG. 2. Constant pressure analysis at (a) 500 hPa and (b) 850 hPa for 0000 20 Jul 1993. Solid contours are height (m MSL) at (a) 60-m intervals and (b) 30 m. (a) The 200-hPa 40 m s^{-1} contour is represented by the thick dashed line. (b) Dashed contours are temperatures at 5°C intervals. Temperature and dewpoint depression in $^\circ\text{C}$ are plotted to the left of the station identifier, with temperatures on top. Wind speeds are in m s^{-1} with one full barb equal to 5 m s^{-1} .

parcel trajectories using a surface temperature of 25°C and the average water vapor in the lowest 500 m indicated that cloud base would be about 680 hPa. The corresponding CAPE was 1022 J kg^{-1} . Several eastern Colorado stations observed cloud bases of about 3 km MSL, or about 700 hPa; thus, the predicted cloud base was a good estimate. Although the CAPE near DEN was rather marginal for the development of strong convection, the 0000 20 July soundings from LBF and DDC

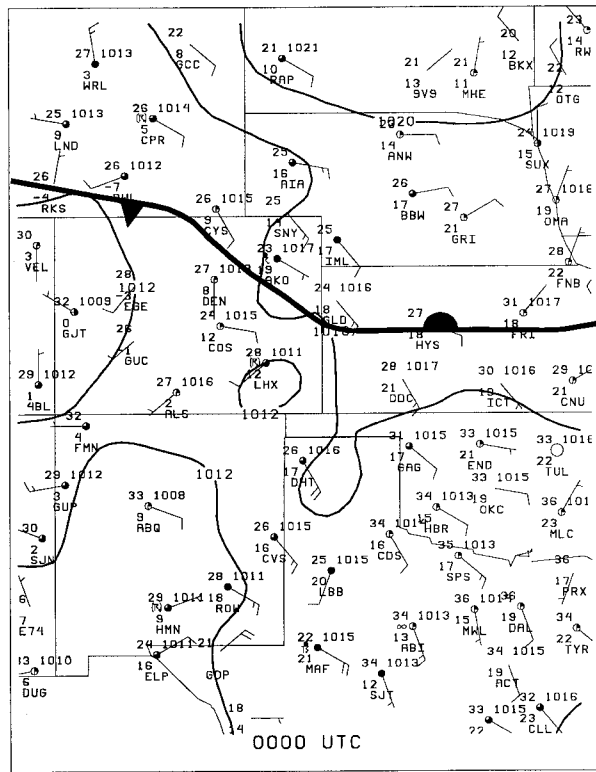


FIG. 3. Surface analyses for 0000 20 Jul 1993. Temperatures ($^{\circ}\text{C}$), weather symbols, and dewpoints ($^{\circ}\text{C}$) are plotted from top to bottom to the left of the station, while NWS mean sea level pressure (MSLP) is plotted to the upper right. Cloud cover in eighths is plotted in the circles. Wind speeds are in m s^{-1} with one full barb equal to 5 m s^{-1} . MSLP is contoured at 4-hPa intervals, and hand-analyzed front has been added.

indicated more energy was available farther east, with CAPE of about 1700 J kg^{-1} .

4. System overview

a. Satellite overview

The MCS investigated here first appeared in the satellite imagery in north-central Colorado at about 2000. By 2100 the cloud tops reached the -54°C level as indicated by the dark gray shading in Fig. 5a. A second region of convection was apparent just north of the Colorado–New Mexico border near the Raton Mesa. Between 2100 and 2330 (Fig. 5b) the northeastern Colorado MCS steadily grew, becoming elongated in a northeast–southwest orientation. The coldest cloud tops were located in the southern and central portions of the anvil, while considerable cloud material advected downstream. In time, the system in southern Colorado propagated almost due south into New Mexico. Additional convection also developed in the Nebraska panhandle along the eastern portions of the Cheyenne Ridge. This eventually became a long-lived MCS that moved

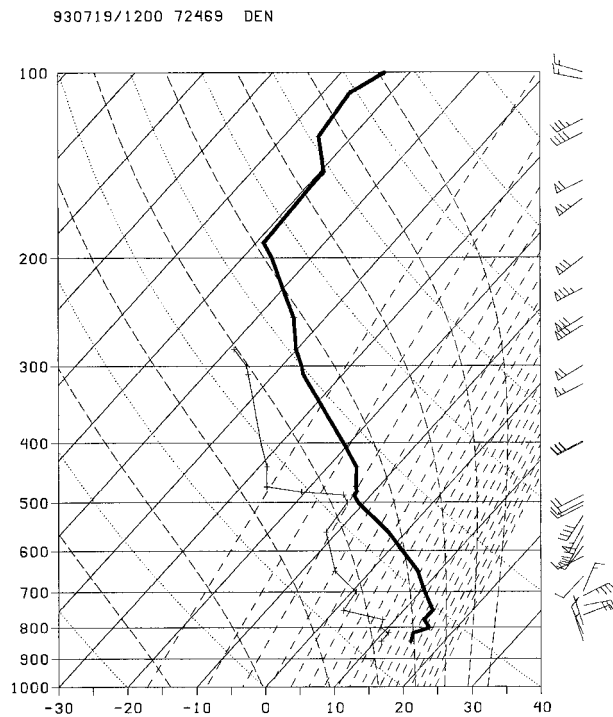


FIG. 4. Skew T - $\log p$ diagram for DEN at 1200 19 Jul 1993. Temperatures and dewpoints in $^{\circ}\text{C}$ are plotted as thick and thin solid lines, respectively. Winds are in m s^{-1} with full bars equal to 5 m s^{-1} and flags equal to 25 m s^{-1} .

through Nebraska, just to the north of the system studied here.

Between 0000 and 0100 20 July (Fig. 5c), the north-eastern Colorado MCS cloud shield blossomed into the typical oval shape with very cold cloud tops in the southwestern quadrant. The western and southern edges of the cloud shield were quite sharp and well defined. However, the eastern and northern cloud edges were much more diffuse, with a broad gradient in the cloud-top temperatures. The convection appeared to pulse somewhat between 0200 and 0300 with new cold clouds developing on the southwestern edge of the system. Although the cloud shield only marginally exceeded the Maddox (1983) MCC time and size criteria, the system remained strong through the night. Up to 12.7 cm of rain fell on parts of western Kansas as the system moved through. By 0600 (Fig. 5d), the cloud shield had partially merged with the system farther north.

b. Radar overview

The first convective cells appeared on radar shortly after local noon, or 1800 UTC, which is typical of Colorado convection (Wetzel et al. 1983; López and Holle 1986). Over the next two hours, two strong cells moved

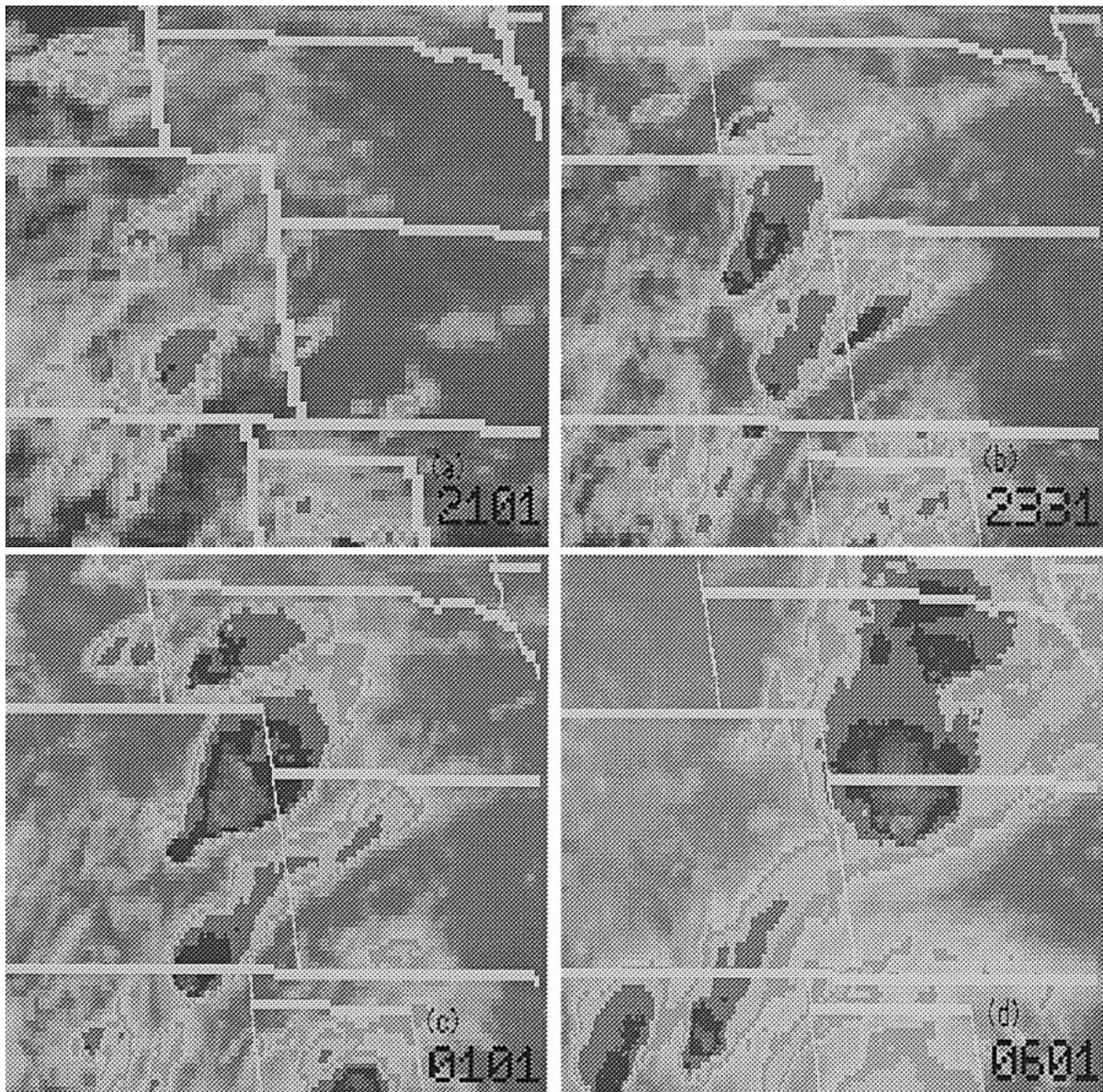


FIG. 5. Enhanced infrared satellite images for (a) 2101 19 Jul, (b) 2331, (c) 0101 20 Jul, and (d) 0601. The IR cloud-top temperatures are shaded at the following increments: -33°C (medium gray), -43°C (light gray), -54°C (dark gray), and -60°C (black). Temperatures colder than -60°C are shaded from black to white (-75°C).

out of the foothills and out onto the Palmer Divide² south of the MH. By 2155 (Fig. 6a), these cells had moved south and east of Denver, where the easternmost cell merged with a developing north–south line of convection. This linear configuration was maintained through the rest of the observation period.

As the line moved east along the Palmer Divide, a meso- β -scale (20–200 km) bow echo developed (Fig.

6b) and persisted from 2209 to 2309. Winds up to 27 m s^{-1} , heavy rain, and hail (NOAA 1993) accompanied the line as it moved through the eastern Doppler lobe. By 2330 (Fig. 6c), however, the line lost most of its bow-echo configuration, and several new convective cells developed ahead of the main squall. These smaller cells moved erratically, drifting toward the northeast or northwest. None of these storms became very strong before merging with the line. Additional convection also developed to the southwest of the main line, most likely on the southern edge of the trailing surface outflow. These cells remained weak until after 0000 20 July, when the line began back-building southwestward. One

² The Palmer Divide is a region of elevated terrain extending eastward from the Colorado Front Range (see Fig. 1).

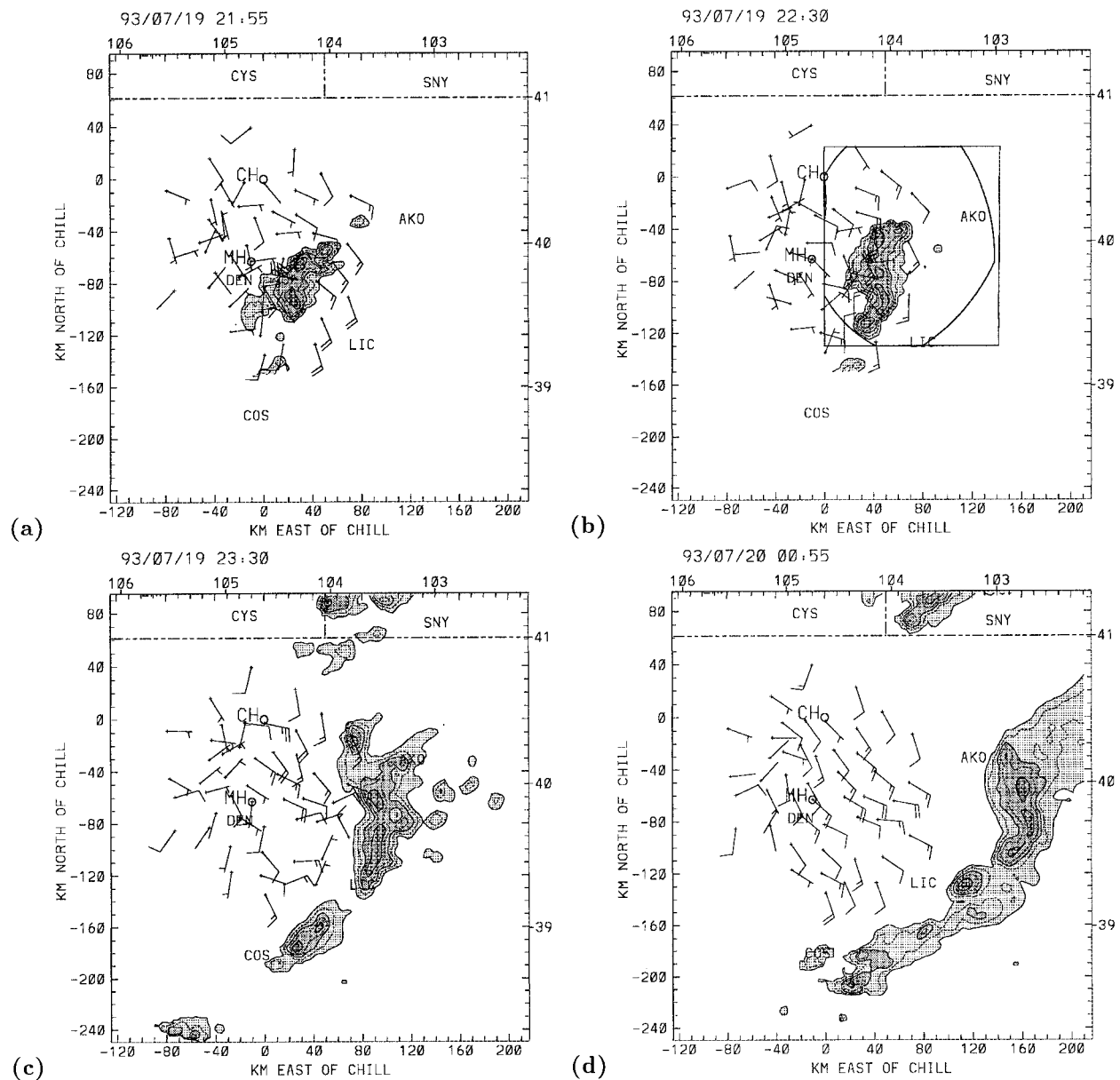


FIG. 6. Surface mesonet and low-level reflectivity analysis for (a) 2155, (b) 2230, (c) 2330, and (d) 0055. Mesonet winds are in m s^{-1} with one full barb equal to 5 m s^{-1} . Reflectivity from the CSU-CHILL at 2 km AGL is contoured at 7.5-dBZ intervals starting at 15 dBZ, with shading increments at 15, 30, and 45 dBZ. (b) The eastern dual-Doppler lobe and analysis grid are plotted. Distance north and east is plotted in km on the left and bottom axes and in latitude and longitude on the right and top.

of these cells was located just east of Limon (LIC) in Fig. 6d. Over the next hour, strong convection continued to develop in this one area, resulting in the elongation of the convective line as each cell moved east. No obvious features were apparent in the surface data to explain these intensified storms, although results from numerical simulations suggest that a localized low-level jet may have formed in that area. Such a situation is not unusual. Maddox et al. (1986) indicated that the most intense convection is often found in the southwestern portion of an MCS. As the MCS propagated

into Kansas, manually digitized radar plots indicate that the strongest convection was concentrated in the southwestern quadrant of the system by 0600.

5. Mesoscale MCS surface environment

a. Convective initiation

The mesonet potential temperatures at 1855 (Fig. 7) were a good predictor for the eventual track of convection. The first convective cells were developing in

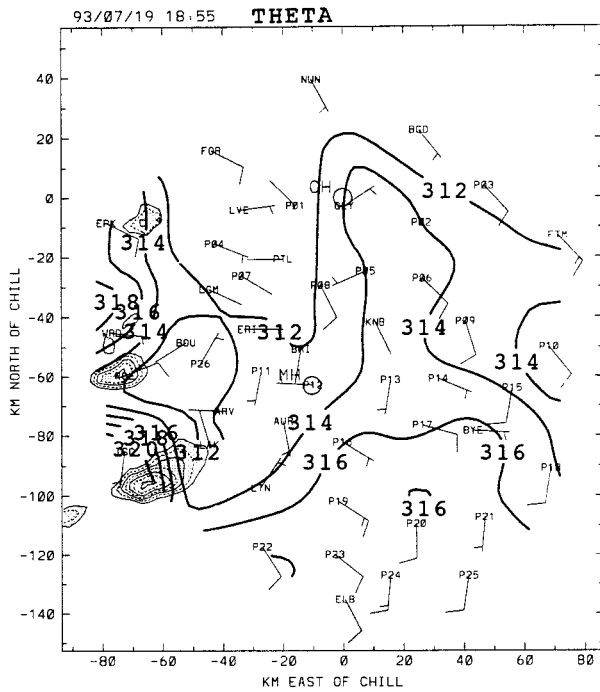


FIG. 7. Surface mesonet analysis for 1855. Winds are in $m s^{-1}$ with one full barb equal to $5 m s^{-1}$. Potential temperatures are objectively analyzed at intervals of 2 K. The x and y axes are km east and north of CHILL, respectively. Reflectivity from the CSU-CHILL at 2 km AGL is contoured at 7.5-dBZ intervals starting at 15 dBZ, with shading increments at 15, 30, and 45 dBZ.

the high foothills at this time, where convective temperature had already been reached. Over the plains, however, potential temperatures were lower, with the lowest values located in the Platte Valley. This area was north of the stationary front (located on the southern border of the mesonet), and thus the air was somewhat cooler. The lower terrain also contributed to the effect.

As convection evolved through the early afternoon, all storms moving eastward into the Platte Valley completely dissipated. Dirks (1969) and Tripoli and Cotton (1989) found that subsidence generally occurred to the lee of the mountains due to the diurnally forced mountain-plains solenoid. Tripoli and Cotton (1989) noted that convection can explosively redevelop east of the suppression zone; however, that did not occur in this case. Surface potential temperatures remained too low, and the capping inversion was too strong for convective redevelopment. On the Palmer Divide, however, higher potential temperatures combined with strong convergence parallel to the divide (Fig. 8a) supported strong convection there. Toth and Johnson (1985) noted that diurnal convergence often occurs along the Palmer Divide, while Klitch et al. (1985) and López and Holle (1986) observed an increased frequency of convection there.

Another localized region of enhanced convergence and cyclonic vorticity, known as the Denver convergence and vorticity zone (DCVZ; Szoke et al. 1984),

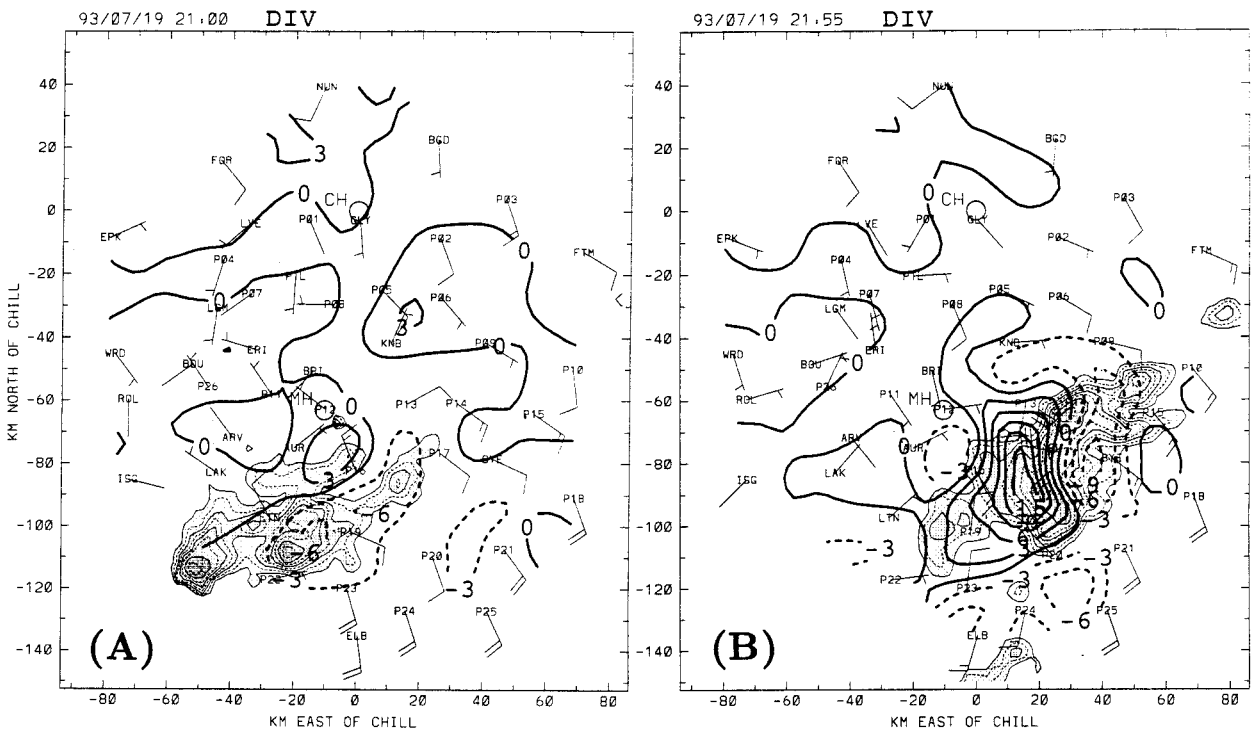


FIG. 8. Surface mesonet and radar reflectivity analyses for (a) 2100 and (b) 2155. Winds are in $m s^{-1}$ with one full barb equal to $5 m s^{-1}$. Divergence (s^{-1}) multiplied by 10^4 is objectively analyzed at intervals of $3 \times 10^{-4} s^{-1}$. Negative contours are dashed. Reflectivity from the CSU-CHILL at 2 km AGL is contoured at 7.5-dBZ intervals starting at 15 dBZ, with shading increments at 15, 30, and 45 dBZ.

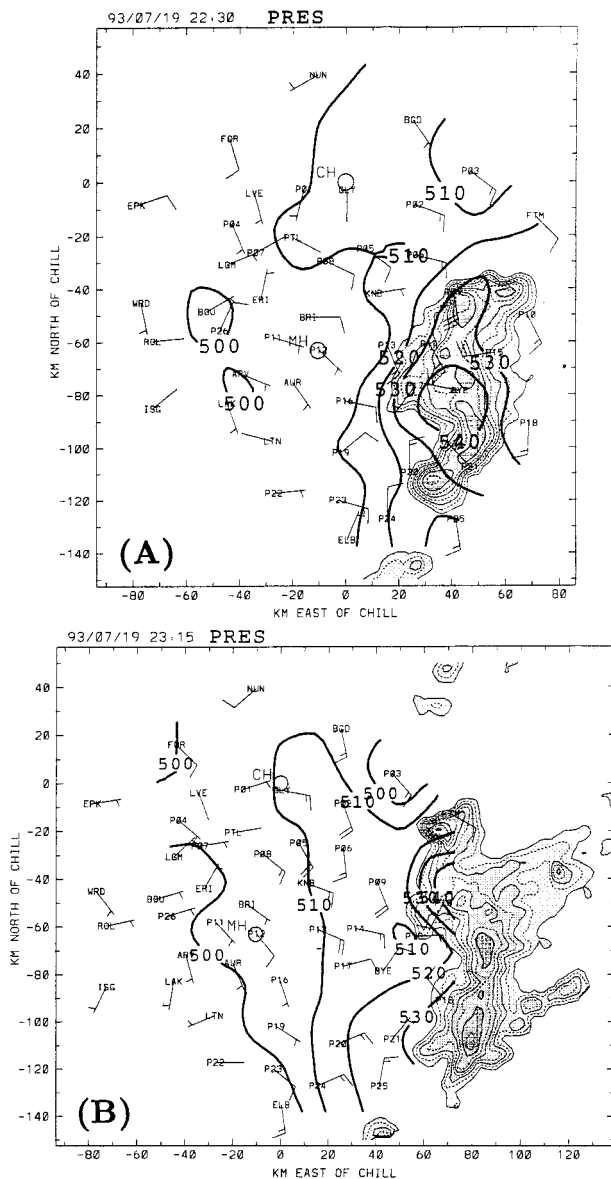


FIG. 9. Surface mesonet and radar reflectivity analyses for (a) 2230 and (b) 2315. Pressure adjusted to 1500 m is objectively analyzed at 1-hPa intervals. All values are plotted with the leading 8 missing, thus 540 = 854.0 hPa. Winds and radar reflectivity are plotted as in Fig. 7.

sometimes develops to the north of the Palmer Divide in southeasterly surface flow. The DCVZ can trigger or enhance convection and is often associated with severe weather (Szoke and Brady 1989). Some question exists as to how much of the preexisting convergence was associated with the DCVZ as opposed to the diurnal solenoids. Although the synoptic wind gradient was southeasterly, mesonet winds were only weakly cyclonic. However, by 2155 (Fig. 8b), strong convergence did develop southeast of Denver. New convection rapidly developed in this convergence zone as the two main cells in Fig. 8a approached. By 2155, the westernmost

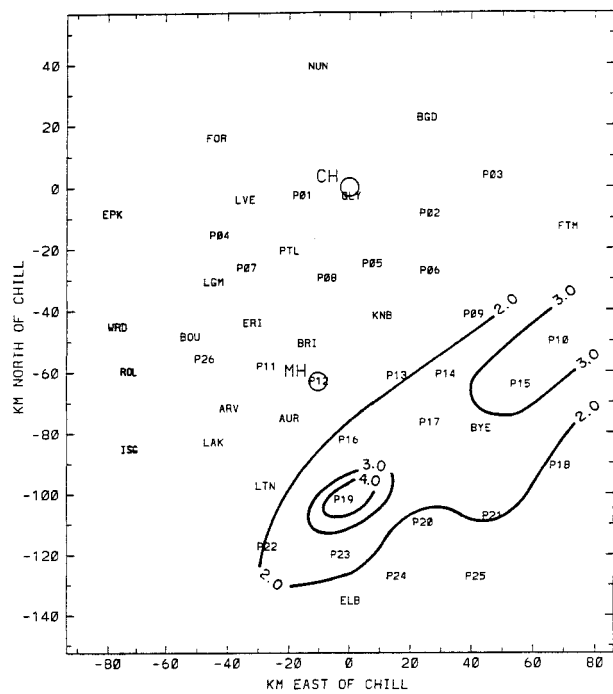


FIG. 10. Mesohigh minus wake low pressure differences. Contours are in 1-hPa increments.

cell had almost completely dissipated, while the eastern cell merged with the growing line. Soon after 2200, the line attained its bow-echo structure as it propagated farther onto the high plains.

b. Growth and evolution

Between 2130 and 2230 (Fig. 9), a surface mesohigh expanded along with the radar echo. No other strong surface convergence zones were detected in the mesonet ahead of the line, and from this point on the most intense convection was associated with the advancing line. This indicates that the gust front was the primary triggering mechanism for convection.

The first signs of a discernible trailing low pressure wake (Fujita 1963; Johnson and Hamilton 1988) appeared by 2230. This “wake low” was characterized by a localized tightening of the pressure gradient at the western edge of the mesohigh rather than a well-defined meso low (Fig. 9a). However a small closed low did develop as the system exited the network (Fig. 9b).

Nachamkin et al. (1994) found that both the mesohigh and the wake low in a growing MCS over Kansas simultaneously strengthened rapidly to form a strong gradient between them. To investigate if this happened in this case, two measurements of the gradient strength were derived from the pressure traces at each mesonet station. First, the absolute difference between the highest mesohigh pressure and the lowest wake pressure was calculated at each station (Fig. 10). Second, the maximum rate of pressure drop within the mesohigh-wake

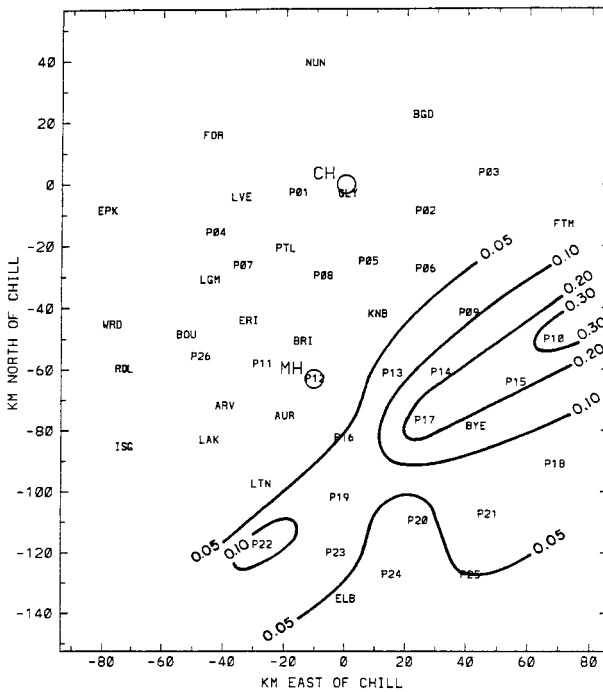


FIG. 11. Mesohigh-wake low gradient strength as measured by maximum pressure fall rates in hPa min^{-1} at each station. Contour intervals are 0.1 hPa min^{-1} , and the $0.05 \text{ hPa min}^{-1}$ contour is also plotted.

low gradient at each station was measured (Fig. 11). For the fall rate calculations, pressure falls at a given station had to last at least 10 min and account for at least 80% of the mesohigh-wake low difference.

The greatest absolute pressure difference was at station P19 (Fig. 10) and was largely due to the passage of a strong cell and its small but intense mesohigh. Although the difference was large, the pressure tendency (Fig. 11) was weak. Strong tendencies did not consistently appear until 2230, when the back edge of the storm passed over station P17. After that, several stations recorded rapid pressure falls, including 10-min pressure drops of 2.7 hPa at P15 and 3.1 hPa at P10. The absolute pressure differences also slightly increased after 2230, with values approaching those recorded at P19. Since the wake low was relatively small, and the trailing edge of the line was between mesonet stations when the surface gradient developed, it is hard to determine if the gradient intensified as rapidly as in Nachamkin et al. (1994). Based on the structure of the greatest pressure drops (Fig. 11), the gradient tightened somewhere between stations P19 and P17, or between the times of 2200 and 2240.

The development and track of the strongest pressure gradient was well correlated with a radar echo notch located near $x = 30, y = -100 \text{ km}$ in Fig. 9a, and $x = 60, y = -70 \text{ km}$ in Fig. 9b. The notch developed shortly before the strong pressure gradients were observed, and was initially located behind the bow echo

in the leading line. A narrow region of stratiform precipitation that had initially been trailing the MCS (Fig. 8b) rapidly dissipated as the notch developed. This combined with the increased wake low gradient indicates the development of strong descent near and north of the notch (Johnson and Hamilton 1988; Stumpf et al. 1991). Notably, once the echo notch became established, there was almost no trailing stratiform anvil. However, the Doppler results in the next section indicate the presence of trailing rear inflow.

6. Doppler-observed structure and evolution

a. The relative wind frame

Determining the extent and structure of the mesoscale perturbations generated by this MCS is one of the main goals of this work. To achieve this, the dual-Doppler winds in both the storm-relative and environment-relative frameworks were investigated, since each approach facilitates a different view of system organization. The storm-relative frame, which is often used in dual-Doppler studies, defines the wind field with respect to the propagating convective system; a constant storm motion is subtracted from the ground-relative winds at all levels. When storm-relative features such as the rear inflow jet or front-to-rear flow become dominant on the mesoscale, it is generally accepted that the system has attained a large degree of mesoscale organization. However, the MCS-altered wind field can also be thought of as a perturbation u' upon the ambient environmental wind $\bar{u}(z)$ such that $u' = u - \bar{u}(z)$, where u is the total wind field. In a sheared environment, coherent mesoscale perturbations can be hidden in the storm-relative framework due to the variation of $\bar{u}(z)$ with height.

Both frameworks have their strengths and weaknesses. Storm motion can be difficult to define, and it can have different definitions in a given system depending on the scale of interest. Since the emphasis in this study is on the scale of the entire MCS, "storm" motion was estimated as the average velocity of all discernible reflectivity cells between 2200 and 0000. Once the convective line formed, it moved with a fairly consistent velocity of 11.8 m s^{-1} from 246° or $(u, v) = (10.8, 4.8) \text{ m s}^{-1}$. The mean environmental wind profile was obtained by averaging data from the 0000 UTC soundings from North Platte, Nebraska, and Dodge City, Kansas (Fig. 12). The Denver sounding was not used because the winds were influenced by convection. Convective influences such as this, as well as strong horizontal gradients in the ambient wind field, can lead to a misdiagnosis in the storm-induced accelerations. In this case, the mid- and upper-tropospheric winds, although rather uniform in direction, generally increased in speed from south to north across the region. Thus the effects on the environment may be underestimated the farther south one looks. The time evolution of the synoptic environment can also be a factor. However, the general pattern

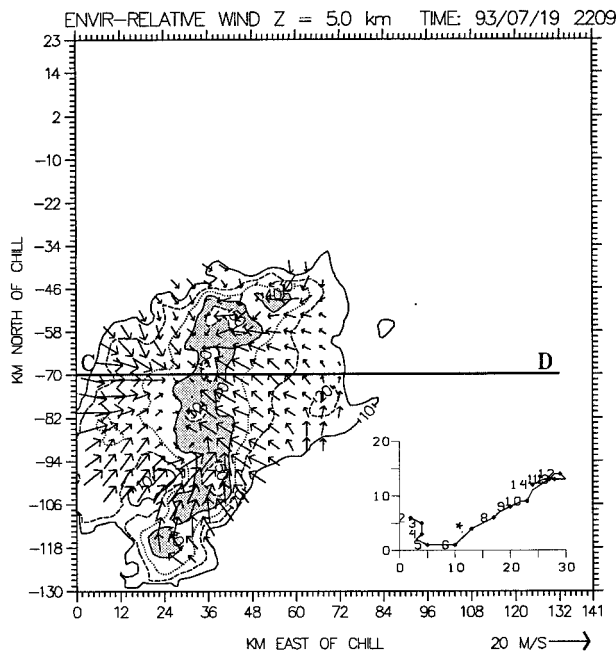


FIG. 12. Dual-Doppler winds and radar reflectivity at $z = 5$ km MSL for the 2209 19 Jul volume. Winds are relative to the mean environmental profile depicted in the hodograph at the lower right. The asterisk denotes the storm motion vector. Winds are in m s^{-1} and the heights are in km MSL. Wind vectors are scaled by the 20 m s^{-1} vector at the lower right. Reflectivity is contoured at 10-dBZ intervals starting at 10 dBZ, while values between 40 and 50 dBZ are shaded. The bold line denotes the position the vertical cross section in Fig. 14.

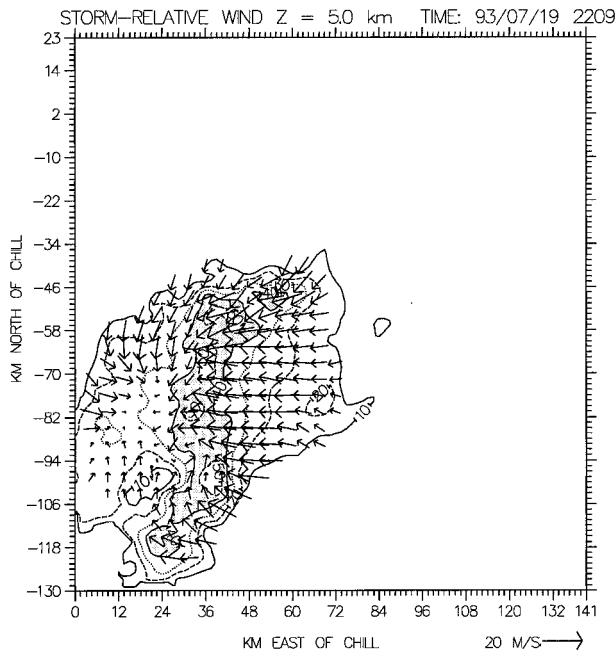


FIG. 13. Dual-Doppler winds and radar reflectivity at $z = 5$ km MSL for the 2209 19 Jul volume. Wind vectors are storm relative and are scaled by the 20 m s^{-1} vector at the lower right. Reflectivity is plotted as in Fig. 12.

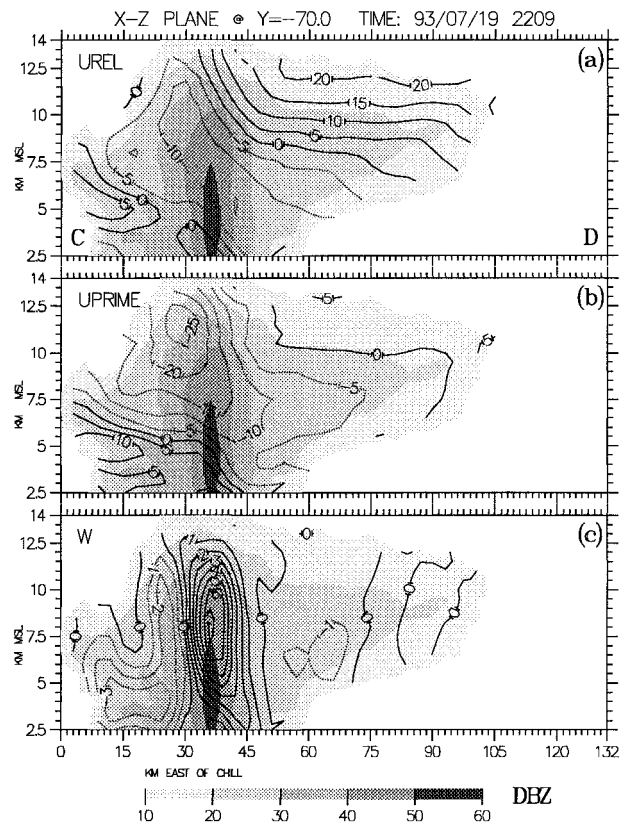


FIG. 14. Vertical cross sections taken at $y = -70$ km in the 2209 Doppler volume. Radar reflectivity is shaded in all plots as defined by the bar. The bold letters at the bottom of (a) correspond to those in Fig. 12. Storm-relative and environment-relative u component winds are contoured at 5 m s^{-1} increments in (a) and (b), respectively. (c) Vertical velocity is contoured at 1 m s^{-1} increments.

during this period was not very progressive and lacked any well-defined short waves; thus, the effect was deemed to be minor.

b. Reflectivity and flow structure

This system displayed considerable mesoscale organization very early in its lifetime. By 2209 (Figs. 12, 13), the basic flow features that were present through the entire analysis had already developed. At $z = 5$ km MSL³ storm-relative flow (Fig. 13) was converging in from all sides, with the strongest inflow on the eastern side of the line. Rear inflow penetrated the MCS along the entire western flank, but the strongest storm-relative rear inflow, up to 10 m s^{-1} , was mostly north of $y = -82$ km. Although the rear inflow was in a region of trailing cloud debris, reflectivities were generally less than 30 dBZ. Cross sections (Fig. 14) reveal that this condensate was of limited extent and shallow compared

³ All heights are MSL.

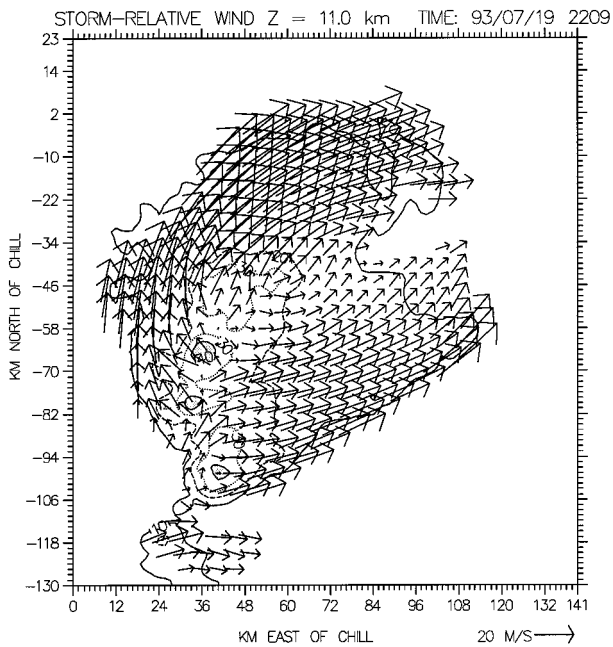


FIG. 15. Dual-Doppler winds and radar reflectivity at $z = 11$ km MSL for the 2209 19 Jul volume. Vectors are storm relative. Reflectivity and vectors are plotted as in Fig. 12.

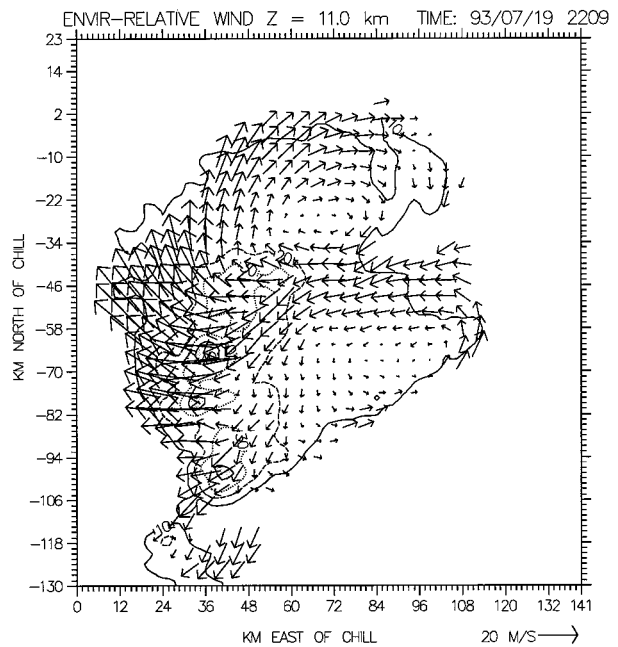


FIG. 16. Dual-Doppler winds and radar reflectivity at $z = 11$ km MSL for the 2209 19 Jul volume. Vectors are relative to the mean environmental winds. Reflectivity and vectors are plotted as in Fig. 12.

to the convection and leading anvil, with echo tops below $z = 10$ km.

The perturbation flow at $z = 5$ km (Fig. 12) was similar to the storm-relative flow in that coherent inward perturbations were present around the entire system. However, the perturbation rear inflow was stronger and more symmetric than its storm-relative counterpart. Conversely, perturbation easterly inflow to the east of the line was weaker at this level than the storm-relative easterlies there.

East–west vertical cross sections of storm-relative winds (Fig. 14a) suggest the dominance of an overturning circulation, with air feeding in from the east at low to midlevels, rising almost vertically in the main updrafts (Fig. 14c) and ejecting eastward in strong outflow. Rear inflow was present, but relatively weak and limited. The perturbation circulations (Fig. 14b), however, tell a different story. The strong upper-tropospheric storm-relative flow ahead of the line was actually not much different than the ambient sounding winds. In fact, at most levels east of the line, perturbation flow was not much greater than 5 m s^{-1} . In contrast, both front-to-rear and rear-to-front perturbations were quite strong to the west of the line. The lack of any strong horizontal velocity gradients at the trailing edge of the reflectivity suggests, as in Klimowski (1994), that these perturbations extended westward into the echo-free air. In essence, a leading-line/trailing-stratiform flow structure was being superimposed upon the ambient flow. This was seemingly independent of the anvil microphysics

as most of the anvil condensate was advecting ahead of the line.

The storm-relative winds at 11 km (Fig. 15) show that anvil condensate was advected farthest east on the northern and southern edges of the MCS, where air was flowing around the system. Weakened winds to the northeast of the convective line center were indicative of obstacle flow. The Froude number ($F = u/Nh$) of the flow approaching the system at $z = 11$ km was estimated using the 0000 20 July Denver sounding and the height of the radar returns. The values of $u = 30 \text{ m s}^{-1}$, $N = 0.01 \text{ s}^{-1}$, and $h \approx 4000 \text{ m}^4$ resulted in a Froude number of about 0.75. This estimate may be large since values of N went up sharply at the tropopause (12 km). However, it still indicates that air should go around the obstacle. Figures 15 and 16 show strong deceleration and blocking of the ambient flow along the entire western side of the system where the winds slowed down and turned mainly northward. The coherent nature of these perturbations is evidence that the convective cells were perturbing the atmosphere together as a whole.

The perturbation winds (Fig. 16) offer additional clues about the nature of the obstacle flow. Two counterrotating vortical perturbations, resembling the wake created by an isolated obstacle in low Froude number flow (Smolarkiewicz and Rotunno 1989; Smith 1989),

⁴ This value was used because observable radar echos extended to 15 km, or 4000 m above the 11-km level.

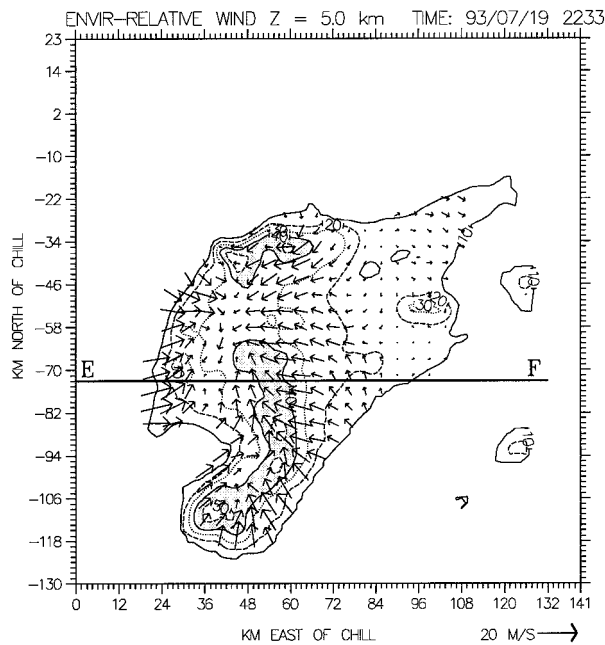


FIG. 17. Dual-Doppler winds and radar reflectivity at $z = 5$ km MSL for the 2233 19 Jul volume. Vectors are relative to the mean environmental winds. Reflectivity and vectors are plotted as in Fig. 12. The bold line denotes the position the vertical cross section in Fig. 19.

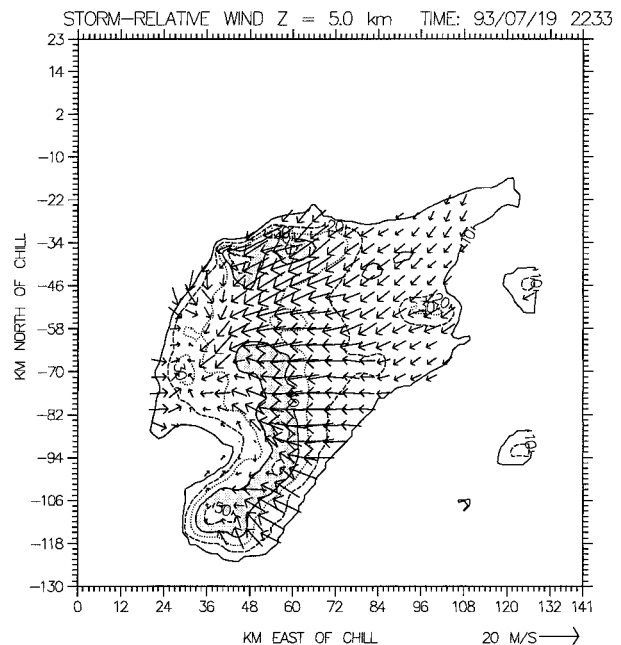


FIG. 18. Dual-Doppler winds and radar reflectivity at $z = 5$ km MSL for the 2233 19 Jul volume. Vectors are storm relative. Reflectivity and vectors are plotted as in Fig. 12.

dominated the anvil. Fujita (1982) documented similar vortical perturbations in the downstream anvil of a severe thunderstorm complex. The dual perturbations in the vorticity field extended between $z = 8$ and $z = 12$ km, although the closed vortices were not apparent below $z = 10$ km.

c. Growth and evolution

As the MCS expanded over the next 1.5 h, the same mesoscale flow structure prevailed. At 2233 (Figs. 17 and 18), midtropospheric flow continued to converge from all directions, with the strongest environment-relative perturbations on the western side. The bow echo in the convective line was well defined, and the reflectivity notch had also grown. Most of the stratiform echo southwest of the line had dissipated. The overall structure was similar to the asymmetric leading-line/trailing-stratiform archetype discussed by Houze et al. (1990). The main exception was the predominance of stratiform echo ahead of the convective line.

Behind the northern half of the convective line, storm-relative easterlies had propagated westward such that strong convergence existed 10–15 km west the line (Figs. 18 and 19). The resulting downward motion (Fig. 19c) was likely enhancing the latent cooling processes (Johnson and Hamilton 1988) in the development of the wake low, as this was the same area where the surface mesohigh–wake low pressure gradient was strengthening. Stumpf et al. (1991) observed a similar configu-

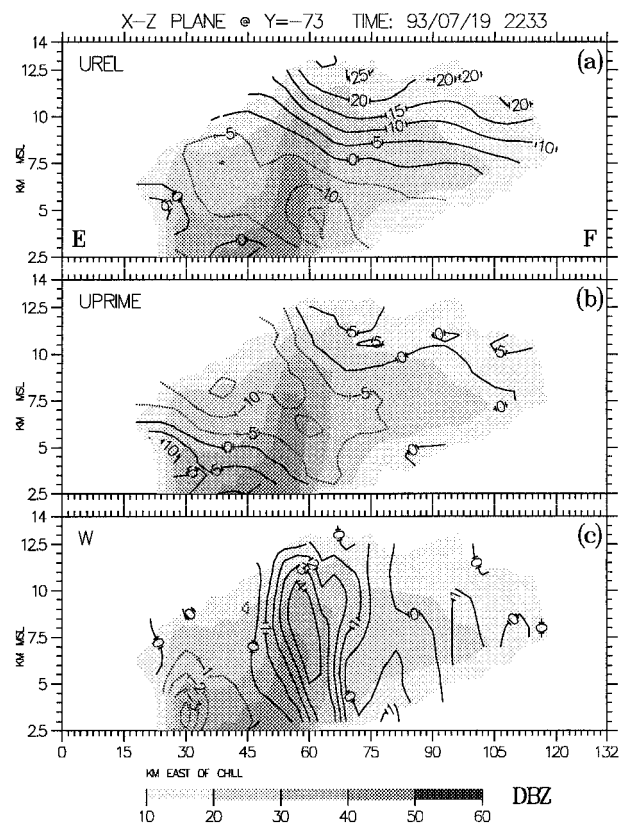


FIG. 19. Vertical cross sections taken at $y = -73$ km in the 2233 Doppler volume. The bold letters at the bottom of (a) correspond to those in Fig. 17. Other details are as in Fig. 14.

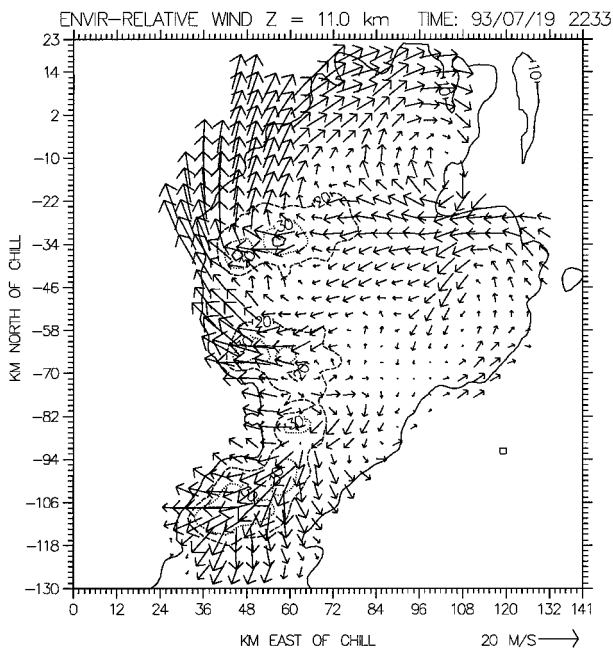


FIG. 20. Dual-Doppler winds and radar reflectivity at $z = 11$ km MSL for the 2233 19 Jul volume. Vectors are relative to the mean environmental winds. Reflectivity and vectors are plotted as in Fig. 12.

ration in a much larger system during the Preliminary Regional Experiment-Stormscale Operational and Research Meteorology. In that case, the strongest meso-high-wake low gradient was also in the northern portions of the MCS in a region where rear inflow westerlies met with deep front-to-rear easterlies. The 19 July case differed from theirs, however, in that no deep trailing stratiform anvil was present. Farther south, the full extent of the rear inflow in the echo notch region was unknown due to the lack of radar returns. Although little storm-relative rear inflow was present at the western edge of the reflectivity in this region (Fig. 18), 5 m s^{-1} westerly perturbation flow did exist at midlevels (Fig. 17).

The upper-tropospheric anvil was still dominated by a blocking pattern, with mainly northward deflection of the upstream flow (Figs. 20 and 21). Retrieved perturbation pressures at 2233 (Fig. 21) typified the structure seen at other times, with the highest values appearing on the upwind (southwestern) side of the system and the lowest values to the north. The strongest mesohigh aloft was well correlated with the most intense convective cells in the southern part of the system, and the strong south-to-north pressure gradient along the western side is consistent with the northward wind acceleration. The pattern suggests that high pressure and front-to-rear velocity perturbations extended westward, outside of the detectable echo.

By 2321 (Fig. 22) the convective line had lost much of its bow-echo characteristics. However, convection re-

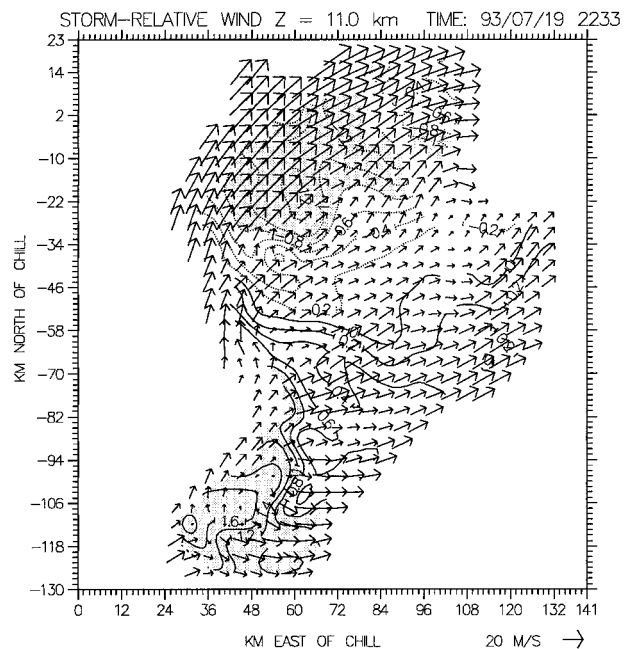


FIG. 21. Dual-Doppler winds and perturbation pressures at $z = 11$ km MSL for the 2233 19 Jul volume. Vectors are storm relative and are scaled by the 20 m s^{-1} vector at the lower right. Note that the scaling is exactly half that of the previous horizontal cross sections. Perturbation pressure is contoured at 0.2-mb intervals, solid (dashed) contours are positive (negative), and values with absolute magnitudes greater than 0.8 are shaded.

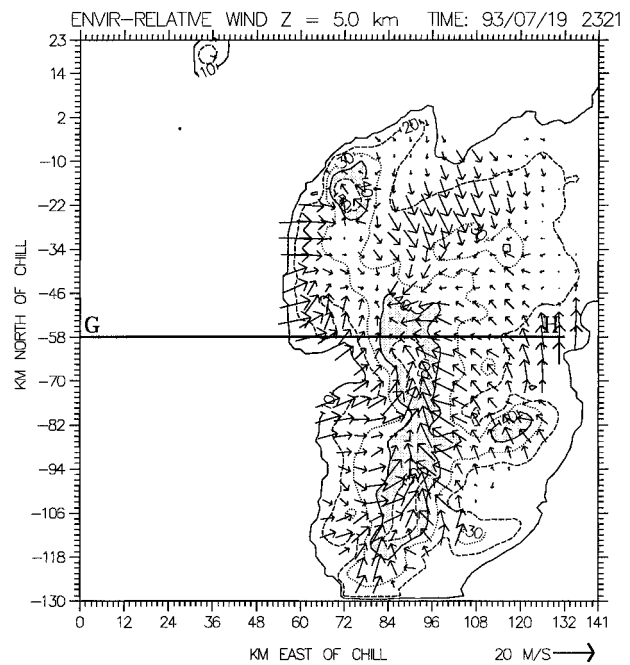


FIG. 22. Dual-Doppler winds and radar reflectivity at $z = 5$ km MSL for the 2321 19 Jul volume. Vectors are relative to the mean environmental winds. Reflectivity and vectors are plotted as in Fig. 12. The bold line denotes the position the vertical cross section in Fig. 23.

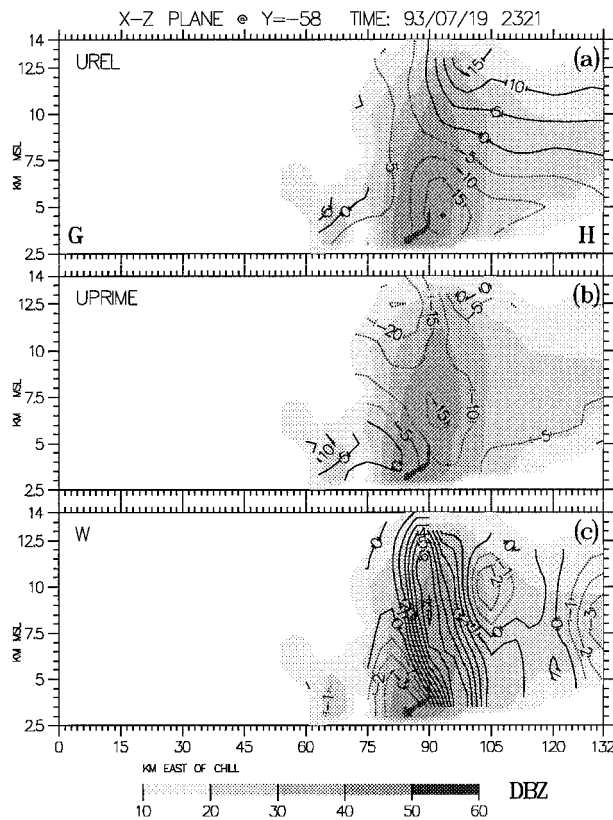


FIG. 23. Vertical cross sections taken at $y = -58$ km in the 2321 Doppler volume. The bold letters at the bottom of (a) correspond to those in Fig. 22. Other details are as in Fig. 14.

mained strong and the rear-echo notch was still present. The strongest environment-relative perturbations continued to be on the western side of the line (Fig. 23). Perturbation westerlies of up to 15 m s^{-1} existed within the rear inflow despite the narrow and shallow trailing stratiform anvil. With the growth of the leading anvil on the northern side of the convective line, midtropospheric flow began converging in from the north and south (Fig. 22). This trend was most evident in the environment-relative winds at $z = 5$ km, although both frameworks indicated it. Inflow on the northern flank of the anvil was similar to an elevated rear inflow jet. The mesoscale structure of the southern flank inflow was less evident due to the embedded convective cells and the poor resolution at far radar ranges.

d. Time series of averaged and integrated quantities

Tripoli and Cotton (1989), McAnelly and Cotton (1992), and McAnelly et al. (1997) hypothesized that meso- β -scale bursts or cycles in the volumetric precipitation rate may be associated with episodes of mesoscale gravity wave generation. These cycles were characterized by an initial burst of convection followed by a partial collapse, that is subsequently followed by a reintensification. Although the radar velocity data were

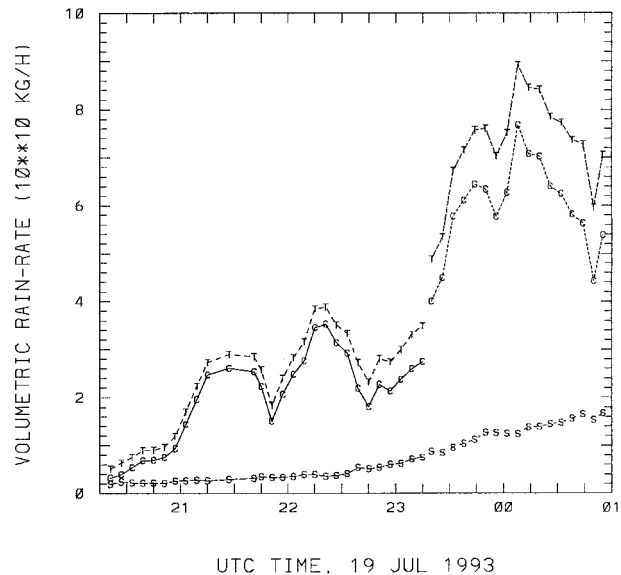


FIG. 24. Time series of MCS volumetric rainfall rate. Rainfall rates on the ordinate are in increments of $10^{10} \text{ kg h}^{-1}$, while time in hours UTC is on the abscissa. Rainfall rates for the total MCS, as well as the convective and stratiform components are labeled by T, C, and S, respectively.

too coarse to resolve any propagating gravity waves, McAnelly et al. (1997) noted that the net effects of the waves can manifest themselves through changes in the reflectivity, average divergence, and vertical mass flux profiles. In general, the convective collapse and re-growth cycle was associated with an increase in the stratiform precipitation, a strengthening and deepening of the midtropospheric convergence, and the development of organized descent in the stratiform region. McAnelly and Cotton (1992) hypothesized that this cycle was an important part of the upscale growth process.

For this study, the MCS-integrated volumetric precipitation rate (Fig. 24) was derived from the lowest two elevation scans in the CSU-CHILL volumes. The Marshall-Palmer relation was used to convert reflectivity to rainfall rates as described by McAnelly and Cotton (1992). These were then summed over all observed radar echo. Separate convective and stratiform precipitation rates were derived by assuming all reflectivity above 35 dBZ was convective. Short-range reflectivity data were available between 2209 and 2345, but as the system propagated out of the network, reflectivities from the long-range scans were used (hence the gap at 2315 in Fig. 24). Despite possible biases due to the use of nonoptimal reflectivity-rainfall relationships or other factors, McAnelly and Cotton (1992) found these calculations provided a reliable indication of the bulk rainfall production tendencies over the entire system.

Three periods of rainfall intensification appeared in Fig. 24. The first occurred between 2100 and 2130 as the system moved out of the mountains and into the DCVZ, the second occurred between 2150 and 2220 as

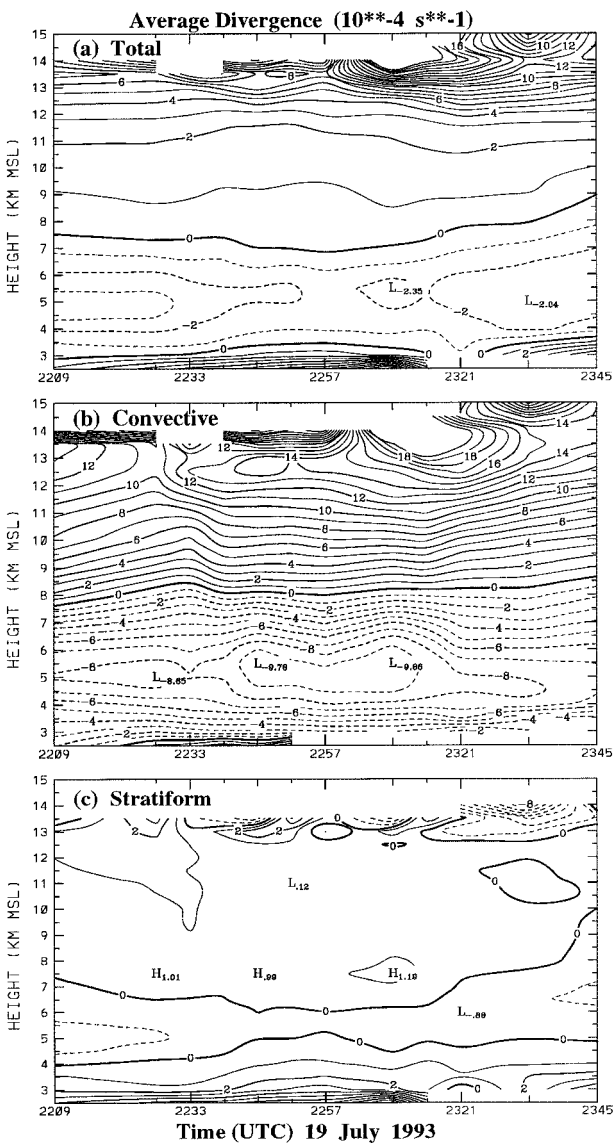


FIG. 25. Time series of vertical profiles of area-averaged divergence for (a) the entire MCS, and (b) the convective and (c) the stratiform portions of the MCS. All contours have been multiplied by a factor of 10^4 . Each Doppler analysis (12 in all) is indicated by a tick mark along the abscissa.

the bow echo intensified, and the third occurred as the system left the dual-Doppler network and came under the influence of the low-level jet. The cycle defined by the second and third intensification periods resembled cycles studied by McAnelly and Cotton (1992) in that the stratiform precipitation rates increased shortly after the decrease in convective intensity. Much of this cycle occurred while the MCS was in the Doppler observation network, thus allowing the average divergence and integrated vertical mass flux fields to be investigated.

Vertical profiles of average divergence (Fig. 25) and integrated vertical mass flux (Fig. 26) were derived for all 12 Doppler volumes. The profiles were considered

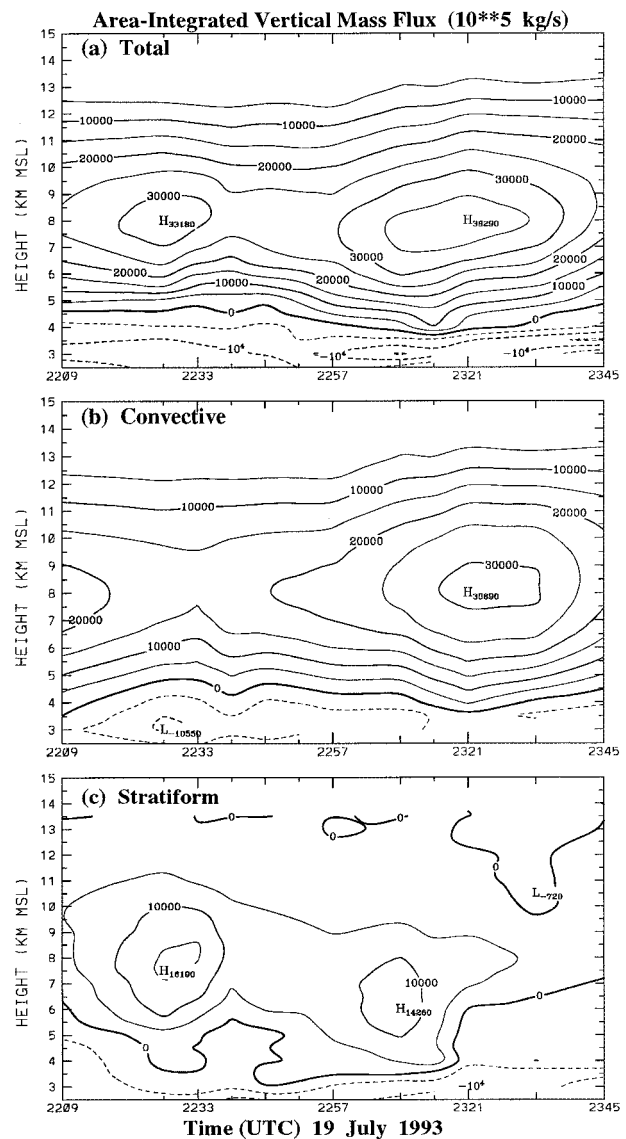


FIG. 26. Time series of vertical profiles of integrated vertical mass flux for (a) the entire MCS, and (b) the convective and (c) the stratiform portions of the MCS. All contours have been multiplied by a factor of 10^{-5} . Each Doppler analysis (12 in all) is indicated by a tick mark along the abscissa.

to be representative at all levels except near storm top (above $z = 12$ km) and near the surface (below 4 km), where the lack of observable echo led to biased values. The integrated mass flux was calculated by assuming that density varied as $\rho = 1.2e^{-0.1z}$, where z is height in kilometers. As in McAnelly et al. (1997), the stratiform and convective components were thresholded using radar-derived vertically integrated liquid water (VIL).⁵

⁵ A reflectivity–liquid water concentration relation, based on the assumptions used in the Marshall–Palmer Z – R relation, was used.

Values greater than 2.5 kg m^{-2} were considered to be convective.

Although the MCS was in its early stages, the MCS-total divergence profiles (Fig. 25a) resembled those in more mature systems. Convergence extended through most of the midtroposphere with a maximum near $z = 5 \text{ km}$, while divergence dominated the upper and lower troposphere. As noted by McAnelly et al. (1997), lower-tropospheric convergence was likely undersampled due to the lack of sufficient scatterers in portions of the updraft clouds that were rain free. Thus, convergence likely extended to lower levels than indicated in Fig. 25. Total convergence deepened after 2309 as the level of nondivergence increased from 7 to 9 km. This mainly resulted from a deepening of convergence in the stratiform region, especially after 2321 (Fig. 25c). The shape of the convective divergence profile (Fig. 25b) changed little through the period, although midlevel values were slightly enhanced between 2239 and 2321. This corresponded to the minimum in the convective rainfall rates in Fig. 24.

The vertical mass flux and volumetric rainfall rate time series shared good qualitative agreement. Increased rainfall rates occurred close to times of strongest total midtropospheric positive mass flux (Fig. 26a). The minimum in the total vertical mass flux between 2233 and 2257 corresponded well with the decreased rainfall rates. The decrease in the strength of the upward mass flux toward the end of the period was likely due to convection moving out of the network by 2345. Interestingly, the strongest upward stratiform mass fluxes occurred around 2233, or shortly after the convective rainfall rate maximum in Fig. 24. This was due to residual upward motions within dissipating convection (with low VIL) that was initially west of the convective line. After this initial maximum, upward mass flux within the stratiform anvil remained quite weak. As the mid-level stratiform convergence profiles deepened after 2321, the downward mass flux in the stratiform anvil also deepened (Fig. 26a).

The increase in midtropospheric convergence and the development of downward mass flux in the stratiform region after 2321 are consistent with the observations of McAnelly et al. (1997). Although the cycle in this system was not as strong as those observed by McAnelly et al. (1997), the stratiform kinematic features did develop within an hour of the initial burst in the convective rainfall rate. These results provide additional evidence suggesting that these cycles are common in developing MCSs. The extent of the gravity wave activity that occurred during the fluctuations in MCS intensity is unknown due to limitations in the resolution of the Doppler data. The perturbation velocities show evidence of rearward propagating gravity waves both before and after the convective burst. This suggests an ongoing process in which convection continually produces gravity wave disturbances that in turn distribute the subsidence heating as they propagate away. The convective bursts them-

selves will result in enhanced gravity wave activity, which in turn can enhance midtropospheric convergence (Mapes 1993). A discussion of the convective-scale kinematics associated with these convective bursts is reserved for Part II.

7. Discussion

The results here indicate that an MCS can generate a subtle but coherent environmental disturbance that may not be easily detected in the storm-relative framework. The storm-relative winds in this case implied that the downstream stratiform anvil resulted from the active injection of condensate and perturbation momentum downstream. However, perturbation winds reveal that condensate was instead passively advecting downstream in the mean environmental flow. In fact, this system was generating environmental wind perturbations much like those found in leading-line/*trailing*-stratiform cases. Although the full extent of these perturbations is unknown due to radar limitations, results from Part II indicate they extended well into the trailing environment.

The development of these perturbations despite the lack of a trailing stratiform anvil strongly suggests the presence of upstream gravity wave propagation. Without a stratiform anvil, mechanisms for midtropospheric rear inflow development discussed by Brown (1979), LeMone (1983), and Smull and Houze (1987) are relatively inactive. The possible exception may be close to the trailing edge of the reflectivity near the wake low, where latent cooling was likely driving significant downdrafts. Leary and Houze (1979) and Smull and Houze (1987) noted that such cooling can aid in the development of storm-relative rear inflow.

Bretherton and Smolarkiewicz (1989), Schmidt and Cotton (1990), Mapes (1993), Johnson et al. (1995), Pandya and Durran (1996), and McAnelly et al. (1997) have all noted that gravity waves generated by precipitating convection can induce front-to-rear and rear-to-front flows well away from the system. In most observational studies, the contribution these waves make to the mesoscale circulation is difficult to measure since many systems are investigated during their mature stage. At that point, processes within the deep stratiform anvil contribute directly to the mesoscale circulations. In the case studied here, the upper-tropospheric shear displaced the anvil condensate downstream. Thus any trailing gravity wave effects were effectively separated from most of the stratiform anvil processes.

One interesting aspect of this case was the relative dominance of the wind perturbations on the trailing side of the system. Pandya and Durran (1996) found that gravity wave energy propagated in very specific directions depending on the shape and orientation of heat source. In general, they found that the majority of the wave energy propagated rearward when (i) the heat source tilted rearward with height and (ii) the majority of the cooling existed at low levels to the rear of the

heating. This is generally the case in most mature systems with well-developed trailing stratiform anvils, but rearward-leaning convection could also produce this structure. Although a full heating budget was not calculated here, the slight rearward lean of the updrafts suggests a similar structure in the heat source (Figs. 14, 19, and 23). The highest reflectivity cores were also consistently on the western side of the updrafts, suggesting that the majority of the cooling occurred at low levels behind the updrafts.

The presence of gravity wave induced circulations suggests that an MCS produces a continuum of disturbances that effect the surrounding environment. When the environmental shear is deep and strong, as it was in this case, Rotunno et al. (1988), Schmidt and Cotton (1990), Weisman (1992), and Grady and Verlinde (1997) have shown that convection tends to remain relatively erect and the formation of a deep trailing anvil is inhibited. However, gravity wave-induced accelerations can provide a more favorable environment for a rearward tilt by reducing the upper-tropospheric shear. Since no trailing anvil developed while the 19 July system was within the Doppler network, it is difficult to determine if the gravity wave perturbations alone were enough to eventually generate a trailing anvil. Conceivably, in conditions of weak upper-tropospheric shear, such accelerations could reverse the storm-relative upper-tropospheric flow and allow for the rearward advection of condensate. The explosive growth phase of this MCS was simulated in Part II of this study, and at that point a significant trailing stratiform anvil did develop. As we shall see, an intense injection of convective outflow aloft, which had little to do with the more linear gravity waves, played a significant role in the development of a trailing anvil.

8. Summary and conclusions

Topography played a major role in the initial development and growth of this MCS. Convection developed in the highest mountains as moist upslope flow became unstable. However, only those storms along the Palmer Divide traversed the mountain-plains solenoid suppression zone without dissipating. This confined convection to a localized area before the convective temperature was reached around most of the region. Much of the environmental instability was thus focused in one intense cluster of storms.

Although this MCS consisted of relatively erect convective cells and a leading stratiform anvil, the environmental perturbations were similar to systems with mature upshear-tilted convection and trailing stratiform anvils. The atmospheric response to convection was characteristic of the propagation of low-frequency gravity wave energy from heat sources with elevated heating maxima. This emphasizes the distinction between the storm-relative and environment-relative wind frameworks. While both are useful, the development of me-

scale circulations in a sheared environment is best viewed with respect to the environmental winds.

Cases like this are rarely examined since the emphasis of most studies is on the mature leading-line/trailing-stratiform system. However, the leading anvil structure may be rather common to high plains systems. Grady and Verlinde (1997) observed it, and leading anvils were frequently observed during the three-year field project.

Although these observations provided much insight, many aspects of this system and its interactions with the surrounding environment remain unknown due to the limitations of the network. Other than soundings and the mesonet, no data were available outside the contiguous MCS anvil. Thus, interactions between the MCS and its surrounding environment could only be inferred from observations from within the system. The coarse resolution mandated by the long baseline made radar detection of the subtle vertical motions at the gravity wave fronts (often less than 1 m s^{-1}) nearly impossible. The model results shown in Part II will offer an opportunity to view the MCS evolution from the perspective of its interactions with the surrounding environment. Although the model contains many simplifications of the atmosphere, comparison with the high-resolution observational dataset offers a high standard of ground truth that is rarely available.

Acknowledgments. Richard Johnson, Roger Pielke, and V. Chandrasekar were members of the Ph.D. committee that guided this research. Steve Rutledge, Pat Kennedy, Dave Brunkow, and Ken Pattison provided data and field project support from the CSU-CHILL. Bob Rilling (NCAR) provided the Mile High data, and Michele Case (NCAR) was helpful with the radar software. Peter Neilley (NCAR) provided mesonet data, while satellite data were obtained from Nan McClurg and CIRA. Brian Bietler (CSU) provided mesoscale forecasts from the RAMS model during the field project. Computer and software support were provided by Donna Chester, Doug Burks, John Blanco, and Steve Finley. Brenda Thompson and Abby Hodges helped with the manuscript preparation. This work was supported by the National Science Foundation, under Grants ATM-9118963, ATM-9420045, ATM-9900929, and through a 20-h minigrant from the CSU-CHILL Cooperative Agreement ATM-8919080.

REFERENCES

- Bell, G. D., and J. E. Janowiak, 1995: Atmospheric circulation associated with the Midwest floods of 1993. *Bull. Amer. Meteor. Soc.*, **76**, 681–695.
- Bluestein, H. B., and M. H. Jain, 1985: Formation of mesoscale lines of precipitation: Severe squall lines in Oklahoma during the spring. *J. Atmos. Sci.*, **42**, 1711–1732.
- Bretherton, C. S., and P. K. Smolarkiewicz, 1989: Gravity waves, compensating subsidence, and detrainment around cumulus clouds. *J. Atmos. Sci.*, **46**, 740–759.
- Brown, J. M., 1979: Mesoscale unsaturated downdrafts driven by

- rainfall evaporation: A numerical study. *J. Atmos. Sci.*, **36**, 313–338.
- Dirks, R., 1969: A theoretical investigation of convective patterns in the lee of the Colorado Rockies. Dept. of Atmospheric Science Paper 145, Colorado State University, 122 pp. [Available from Department of Atmospheric Science, Colorado State University, Fort Collins, CO 80523.]
- Fortune, M. A., W. R. Cotton, and R. L. McAnelly, 1992: Frontal wave-like evolution in some mesoscale convective complexes. *Mon. Wea. Rev.*, **120**, 1279–1300.
- Fujita, T. T., 1963: Analytical mesometeorology: A review. *Severe Local Storms, Meteor. Monogr.*, No. 27, Amer. Meteor. Soc., 77–125.
- , 1982: Principle of stereoscopic height computations and their applications to stratospheric cirrus over severe storms. *J. Meteor. Soc. Japan*, **60**, 355–368.
- Gal-Chen, T., 1978: A method for the initialization of the anelastic equations: Implications for matching models with observations. *Mon. Wea. Rev.*, **106**, 587–606.
- , and C. E. Hane, 1981: Retrieving buoyancy and pressure fluctuations from Doppler radar observations: A status report. *Recent Progress in Radar Meteorology, Atmospheric Technology*, No. 13, NCAR, 98–104.
- Grady, R. L., and J. Verlinde, 1997: Triple-Doppler analysis of a discretely propagating long-lived High Plains squall line. *J. Atmos. Sci.*, **54**, 2729–2748.
- Houze, R. A., Jr., S. A. Rutledge, M. I. Biggerstaff, and B. F. Smull, 1989: Interpretation of Doppler weather radar displays of mid-latitude mesoscale convective systems. *Bull. Amer. Meteor. Soc.*, **70**, 608–619.
- , B. F. Smull, and P. Dodge, 1990: Mesoscale organization of springtime rainstorms in Oklahoma. *Mon. Wea. Rev.*, **118**, 613–654.
- Johnson R. H., and P. J. Hamilton, 1988: The relationship of surface pressure features to the precipitation and airflow structure of an intense midlatitude squall line. *Mon. Wea. Rev.*, **116**, 1444–1472.
- , B. D. Miner, and P. E. Ciesielski, 1995: Circulations between mesoscale convective systems along a cold front. *Mon. Wea. Rev.*, **123**, 585–599.
- Klimowski, B. A., 1994: Initiation and development of rear inflow within the 28–29 June 1989 North Dakota mesoconvective system. *Mon. Wea. Rev.*, **122**, 765–779.
- Klitch, M. A., J. F. Weaver, F. P. Kelly, and T. H. Vonder Haar, 1985: Convective cloud climatologies constructed from satellite imagery. *Mon. Wea. Rev.*, **113**, 326–337.
- Lafore, J., and M. W. Moncrieff, 1989: A numerical investigation of the organization and interaction of the convective and stratiform regions of tropical squall lines. *J. Atmos. Sci.*, **46**, 521–544.
- Laing, A. G., 1997: The large scale environment of mesoscale convective complexes: Comparisons with other deep convective weather systems. Preprints, *22d Conf. on Hurricanes*, Fort Collins, CO, Amer. Meteor. Soc., 415–416.
- Leary, C. A., and R. A. Houze Jr., 1979: Melting and evaporation of hydrometeors in precipitation from the anvil clouds of deep tropical convection. *J. Atmos. Sci.*, **36**, 669–679.
- Leise, J. A., 1981: A multidimensional scale-telescoped filter and data extension package. NOAA Tech. Memo. ERL WPL-82, Wave Propagation Lab., Boulder CO, 20 pp. [NTIS N82-31994.]
- LeMone, M. A., 1983: Momentum transport by a line of cumulonimbus. *J. Atmos. Sci.*, **40**, 1815–1834.
- López, R. E., and R. L. Holle, 1986: Diurnal and spatial variability of lightning activity in northeastern Colorado and central Florida during the summer. *Mon. Wea. Rev.*, **114**, 1288–1312.
- Maddox, R. A., 1980: Mesoscale convective complexes. *Bull. Amer. Meteor. Soc.*, **61**, 1374–1387.
- , 1983: Large-scale meteorological conditions associated with midlatitude, mesoscale convective complexes. *Mon. Wea. Rev.*, **111**, 1475–1493.
- , K. W. Howard, D. L. Bartels, and D. M. Rodgers, 1986: Mesoscale convective complexes in the middle latitudes. *Mesoscale Meteorology and Forecasting*, P. S. Ray, Ed., Amer. Meteor. Soc., 390–413.
- Mapes, B. E., 1993: Gregarious tropical convection. *J. Atmos. Sci.*, **50**, 2026–2037.
- McAnelly, R. L., and W. R. Cotton, 1986: Meso- β -scale characteristics of an episode of meso- α -scale convective complexes. *Mon. Wea. Rev.*, **114**, 1740–1770.
- , and —, 1992: Early growth of mesoscale convective complexes: A meso- β -scale cycle of convective precipitation? *Mon. Wea. Rev.*, **120**, 1851–1877.
- , J. E. Nachamkin, W. R. Cotton, and M. E. Nicholls, 1997: Upscale evolution of MCSs: Doppler radar analysis and analytical investigation. *Mon. Wea. Rev.*, **125**, 1083–1110.
- Miller, L. J., C. G. Mohr, and A. J. Weinheimer, 1986: The simple rectification to Cartesian space of folded radical velocities from Doppler radar sampling. *J. Atmos. Oceanic Technol.*, **3**, 162–174.
- Mohr, C. G., L. J. Miller, R. L. Vaughn, and H. W. Frank, 1986: The merger of mesoscale datasets into a common Cartesian format for efficient and systematic analyses. *J. Atmos. Oceanic Technol.*, **3**, 143–161.
- Nachamkin, J. E., 1998: Observational and numerical analysis of the genesis of a mesoscale convective system. Ph.D. dissertation, Dept. of Atmospheric Science Paper 643, Colorado State University, 219 pp. [Available from Dept. of Atmospheric Science, Colorado State University, Fort Collins, CO 80523.]
- , and W. R. Cotton, 2000: Interactions between a developing mesoscale convective system and its environment. Part II: Numerical simulation. *Mon. Wea. Rev.*, **128**, 1225–1244.
- , R. L. McAnelly, and W. R. Cotton, 1994: An observational analysis of a developing mesoscale convective complex. *Mon. Wea. Rev.*, **122**, 1168–1188.
- Nicholls, M. E., R. A. Pielke, and W. R. Cotton, 1991: Thermally forced gravity waves in an atmosphere at rest. *J. Atmos. Sci.*, **48**, 1869–1884.
- NOAA, 1993: *Storm Data*. Vol. 35, No. 7, National Oceanic and Atmospheric Administration, Asheville, NC, 300 pp.
- Oye R., and R. Carbone, 1981: Interactive Doppler editing software. Preprints, *20th Conf. on Radar Meteorology*, Boston, MA, Amer. Meteor. Soc., 683–689.
- Pandya, R. D., and D. Durran, 1996: The influence of convectively generated thermal forcing on the mesoscale circulation around squall lines. *J. Atmos. Sci.*, **53**, 2925–2951.
- , —, and C. Bretherton, 1993: Comments on “Thermally forced gravity waves in an atmosphere at rest.” *J. Atmos. Sci.*, **50**, 4097–4101.
- Parsons, D. B., C. G. Mohr, and T. Gal-Chen, 1987: A severe frontal rainband. Part III: Derived thermodynamic structure. *J. Atmos. Sci.*, **44**, 1615–1631.
- Pratte, J. F., J. H. van Andel, D. G. Ferraro, R. W. Gagnon, S. M. Maher, and G. L. Blair, 1991: NCAR’s Mile High meteorological radar. Preprints, *25th Conf. on Radar Meteorology*, Paris, France, Amer. Meteor. Soc., 863–866.
- Rosby, C. G., 1938: Mutual adjustment of pressure and velocity distributions in certain simple current systems. *J. Mar. Res.*, **2**, 239–263.
- Rotunno, R., J. B. Klemp, and M. L. Weisman, 1988: A theory for strong, long-lived squall lines. *J. Atmos. Sci.*, **45**, 463–485.
- Rutledge, S. A., P. C. Kennedy, and D. A. Brunkow, 1993: Use of the CSU-CHILL radar in radar meteorology education at Colorado State University. *Bull. Amer. Meteor. Soc.*, **74**, 25–31.
- Schmidt, J. M., and W. R. Cotton, 1990: Interactions between upper and lower tropospheric gravity waves on squall line structure and maintenance. *J. Atmos. Sci.*, **47**, 1205–1222.
- Smith, R. B., 1989: Comment on “Low Froude number flow past three-dimensional obstacles. Part I: Baroclinically generated lee vortices.” *J. Atmos. Sci.*, **46**, 3611–3613.
- Smolarkiewicz, P. K., and R. Rotunno, 1989: Low Froude number flow past three-dimensional obstacles. Part I: Baroclinically generated lee vortices. *J. Atmos. Sci.*, **46**, 1154–1164.

- Smull, B. F., and R. A. Houze Jr., 1987: Rear inflow in squall lines with trailing stratiform precipitation. *Mon. Wea. Rev.*, **115**, 2869–2889.
- , and J. A. Augustine, 1993: Multiscale analysis of a mature mesoscale convective complex. *Mon. Wea. Rev.*, **121**, 103–132.
- Stumpf, G. J., R. H. Johnson, and B. F. Smull, 1991: The wake low in a midlatitude mesoscale convective system having complex convective organization. *Mon. Wea. Rev.*, **119**, 134–158.
- Szoke, E. J., and R. H. Brady, 1989: Forecasting implications of the 26 July 1985 northeastern Colorado tornadic thunderstorm case. *Mon. Wea. Rev.*, **117**, 1834–1860.
- , M. L. Weisman, J. M. Brown, F. Caracena, and T. W. Schlatter, 1984: A subsynoptic analysis of the Denver tornado of 3 June 1981. *Mon. Wea. Rev.*, **112**, 790–808.
- Toth, J. J., and R. H. Johnson, 1985: Summer surface flow characteristics over northeastern Colorado. *Mon. Wea. Rev.*, **113**, 1458–1469.
- Trier, S. B., and D. B. Parsons, 1993: Evolution of environmental conditions preceding the development of a nocturnal mesoscale convective complex. *Mon. Wea. Rev.*, **121**, 1078–1098.
- Tripoli, G., and W. R. Cotton, 1989: A numerical study of an observed orogenic mesoscale convective system. Part I: Simulated genesis and comparison with observations. *Mon. Wea. Rev.*, **117**, 273–304.
- Weisman, M. L., 1992: The role of convectively generated rear-inflow jets in the evolution of long-lived mesoconvective systems. *J. Atmos. Sci.*, **49**, 1826–1847.
- Wetzel, P. J., W. R. Cotton, and R. L. McAnelly, 1983: A long-lived mesoscale convective complex. Part II: Evolution and structure of the mature complex. *Mon. Wea. Rev.*, **111**, 1919–1937.